

MID-INFRARED EXTINCTION MAPPING OF INFRARED DARK CLOUDS. II. THE STRUCTURE OF MASSIVE STARLESS CORES AND CLUMPS

MICHAEL J. BUTLER

Dept. of Astronomy, University of Florida, Gainesville, FL 32611, USA

JONATHAN C. TAN

Depts. of Astronomy & Physics, University of Florida, Gainesville, FL 32611, USA

Draft version June 20, 2018

ABSTRACT

We develop the mid-infrared extinction (MIREX) mapping technique of Butler & Tan (2009, Paper I), presenting a new method to correct for the Galactic foreground emission based on observed saturation in independent cores. Using *Spitzer* GLIMPSE 8 μm images, this allows us to accurately probe mass surface densities, Σ , up to $\simeq 0.5 \text{ g cm}^{-2}$ with $2''$ resolution and mitigate one of the main sources of uncertainty associated with Galactic MIREX mapping. We then characterize the structure of 42 massive starless and early-stage cores and their surrounding clumps, selected from 10 infrared dark clouds (IRDCs), measuring $\Sigma_{\text{cl}}(r)$ from the core/clump centers. We first assess the properties of the core/clump at a scale where the total enclosed mass as projected on the sky is $M_{\text{cl}} = 60 M_{\odot}$. We find these objects have a mean radius of $R_{\text{cl}} \simeq 0.1 \text{ pc}$, mean $\bar{\Sigma}_{\text{cl}} = 0.3 \text{ g cm}^{-2}$ and, if fit by a power law density profile $\rho_{\text{cl}} \propto r^{-k_{\rho,\text{cl}}}$, a mean value of $k_{\rho,\text{cl}} = 1.1$. If we assume a core is embedded in each clump and subtract the surrounding clump envelope to derive the core properties, we find a mean core density power law index of $k_{\rho,c} = 1.6$. We repeat this analysis as a function of radius and derive the best-fitting power law plus uniform clump envelope model for each of the 42 core/clumps. The cores have typical masses of $M_c \sim 100 M_{\odot}$ and $\bar{\Sigma}_c \sim 0.1 \text{ g cm}^{-2}$, and are embedded in clumps with comparable mass surface densities. We also consider Bonnor-Ebert density models, but these do not fit the observed Σ profiles as well as power laws. We conclude massive starless cores exist and are well-described by singular polytropic spheres. Their relatively low values of Σ and the fact that they are IR dark may imply that their fragmentation is inhibited by magnetic fields rather than radiative heating. Comparing to massive star-forming cores and clumps, there is tentative evidence for an evolution towards higher densities and steeper density profiles as star formation proceeds.

Subject headings: ISM: clouds, dust, extinction — stars: formation

1. INTRODUCTION

Characterizing the initial conditions of massive star formation is important for distinguishing between various theoretical models. For example, McKee & Tan (2002, 2003, hereafter MT03) have presented the “Turbulent Core Accretion Model”, which assumes that massive stars (including binaries and other low-order multiple systems) form from massive starless *cores* in a manner that can be considered a scaled-up version of the standard theory of low-mass star formation (Shu, Adams, & Lizano 1987). The core undergoes global collapse to feed a central accretion disk. These massive starless cores are also assumed to be near virial equilibrium and in approximate pressure equilibrium with the surrounding *clump* environment, whose pressure is likely to be set by the self-gravitating weight of the gas, $P_{\text{cl}} \simeq G\Sigma_{\text{cl}}^2$, where Σ_{cl} is the mass surface density of the clump. The clump is defined to be the gas cloud that fragments to form a star cluster. Observed regions of massive star formation, including revealed massive star clusters where this activity occurred recently, have high values of $\Sigma_{\text{cl}} \sim 1 \text{ g cm}^{-2}$ (but with a dispersion of about a factor of 10), implying large values of $P_{\text{cl}}/k \gtrsim 10^8 \text{ K cm}^{-3}$.

A massive, virialized core in pressure equilibrium with this environment cannot be supported by thermal pressure, given observed temperatures of $T \sim 10 - 20 \text{ K}$, and so must be supported by some form of nonthermal pressure, i.e. turbulence or magnetic fields. Since massive stars are “rare”, in the sense that they constitute only a small mass fraction, $\sim 5 - 10\%$, of the observed initial stellar mass function, then massive starless cores that will eventually form massive stars are also expected to be rare. Most massive structures are likely to fragment into clusters of lower-mass stars. We anticipate that preventing fragmentation of massive starless cores likely involves magnetic fields being strong enough such that the core mass is approximately equal to a magnetic critical mass and substructures are magnetically subcritical. Krumholz & McKee (2008) have argued fragmentation is prevented by radiative heating from surrounding low-mass protostars, which requires them to have high accretion rates and thus for the clump to have a high value of $\Sigma \gtrsim 1 \text{ g cm}^{-2}$ in order to form massive stars. There is no such constraint if magnetic fields prevent fragmentation.

MT03 modeled massive cores as singular polytropic spheres, with a power law density distribution of $\rho_c \propto r^{-k_{\rho,c}}$. There were few observational constraints on this density distribution, so MT03 assumed cores were part of a self-similar hierarchy of structure also shared by their surrounding clumps, where observations suggested $k_{\rho,\text{cl}} \simeq 1.5$ (e.g. van der

Tak et al. 2000; Beuther et al. 2002; Mueller et al. 2002). The parameters of a fiducial massive core make it clear why it is difficult to measure the structure observationally. For a $60M_{\odot}$ core embedded near the center of a clump with mean $\Sigma_{\text{cl}} = 1 \text{ g cm}^{-2}$, the radius is $R_c = 0.057M_{c,60}^{1/2}(\Sigma_{\text{cl}}/1 \text{ g cm}^{-2})^{-1/2}$ pc. At typical distances, $\gtrsim 2$ kpc, this radial size corresponds to $\lesssim 5.9''$.

Until recently, measurements of mass surface densities of $\sim 1 \text{ g cm}^{-2}$ (equivalent to $N_{\text{H}} = 4.27 \times 10^{23} \text{ cm}^{-2}$ or $A_V = 230$ mag) were based mostly on mm dust continuum measurements, which require knowing the dust emissivity, dust temperature and dust-to-gas ratio. In particular, the dust emissivity and temperature may be expected to vary along the line of sight through a dense cloud. For total power observations with single dish telescopes, resolutions have been limited to $\sim 10''$, e.g. the diffraction limit of a 30 m telescope at 1.2 mm. Rathborne et al. (2006) carried out a study of this emission from 38 Galactic Infrared Dark Clouds (IRDCs) (these types of clouds are described in more detail below). The above considerations show that we do not expect their results to be able to resolve the scale of individual massive cores in high pressure environments, but are better suited to studying the properties of clumps that might form whole star clusters. Higher angular resolution has been achieved with interferometric observations, but these have been possible only towards relatively limited samples of objects, many of which are already in the process of forming a star (e.g. Bontemps et al. 2010).

The advent of space-based, MIR, high-photometric-accuracy, imaging surveys of the Galactic plane has opened up a new way to probe high mass surface density structures. Indeed, these cold, high Σ structures were first identified as ‘‘Infrared Dark Clouds’’ from analysis of *Infrared Space Observatory* (ISO; Pérault et al. 1996) and the *Midcourse Space Experiment* (MSX; Egan et al. 1998) imaging data. With the *Spitzer Space Telescope*, more precise and higher angular resolution data became available. This led Butler & Tan (2009, hereafter BT09 or Paper I) to attempt to develop MIR extinction (MIREX) mapping as a precision technique for probing high mass surface density regions.

BT09 adopted the Ossenkopf & Henning (1994) thin ice mantle coagulated (for 10^5 yr at densities of 10^6 cm^{-3} or equivalently for $\sim 10^6$ yr at densities of $\sim 10^5 \text{ cm}^{-3}$) dust model for their fiducial analysis and a gas-to-(refractory component)-dust mass ratio of 156 (slightly higher than the value of 141 estimated by Draine (2011) from depletion studies). With these values the opacity per unit gas mass in the IRAC band 4 at $\sim 8 \mu\text{m}$ of a source with a spectrum typical of Galactic diffuse MIR emission is $\kappa_{8\mu\text{m}} = 7.48 \text{ cm}^2 \text{ g}^{-1}$. The fiducial value adopted by BT09 and in this paper is $\kappa_{8\mu\text{m}} = 7.5 \text{ cm}^2 \text{ g}^{-1}$ so that

$$\tau_{8\mu\text{m}} = \kappa_{8\mu\text{m}}\Sigma = 7.5 \left(\frac{\Sigma}{\text{g cm}^{-2}} \right). \quad (1)$$

From the variety of dust models considered by BT09, we expect $\sim 30\%$ uncertainties in the absolute value of $\kappa_{8\mu\text{m}}$. Within a particular IRDC, we can expect some systematic variation in $\kappa_{8\mu\text{m}}$ due to different degrees of ice mantle growth, but these should be at most $\sim 20\%$ (Ossenkopf & Henning 1994), and probably much less after averaging over conditions on a line of sight through the cloud.

Apart from the choice of MIR opacity, there are two main sources of uncertainty involved in MIR extinction mapping. First, the intensity of the MIR emission behind the cloud is assumed to be smooth and must be estimated by extrapolation from nearby regions that are assumed to be extinction free. BT09 estimated that the extrapolation could lead to flux uncertainties of about 10%, corresponding to errors in $\Sigma \simeq 0.01 \text{ g cm}^{-2}$, given fiducial dust models. This is a minimum Σ , below which MIR extinction mapping becomes unreliable. These problems of background estimation can be reduced by choosing IRDCs that are in regions of the Galactic plane where the observed surrounding emission is relatively constant and smooth around the cloud. One systematic bias that we expect to be present is caused by the fact that there will typically be some cloud material in the ‘‘envelope’’ region around the IRDC where extinction was assumed to be zero. From studies of CO emission around IRDCs (Hernandez & Tan 2011; Hernandez et al. 2011) we estimate that this envelope typically has $\Sigma \simeq 0.01 \text{ g cm}^{-2}$. This is an additional reason why MIR extinction mapping becomes unreliable at low values of Σ . This problem can be addressed by combining MIR and NIR extinction mapping techniques (Kainulainen et al. 2011; Kainulainen & Tan, in prep.) The second major source of uncertainty is caused by foreground MIR emission along our line of sight to the IRDC. Neglecting this causes us to underestimate τ and thus Σ . The effect can be minimized by choosing IRDCs that are relatively nearby, as was done by BT09. BT09 also tried to estimate the expected amount of foreground emission assuming it comes from a smoothly distributed population of small dust grains heated by massive stars that follow an exponential distribution in the Galaxy. For a cloud at a distance of 5 kpc at a Galactic longitude of $l \sim 30^\circ$, we estimate that 27% of the observed Galactic diffuse emission is from material in front of the cloud. For a part of the cloud that has Σ estimated to be $\sim 0.1 \text{ g cm}^{-2}$ in the absence of a foreground correction, applying this correction raises Σ by about a factor of two. If this foreground correction is not applied then the largest values of Σ that can be derived are only $\sim 0.2 \text{ g cm}^{-2}$. This model-dependent estimate of the foreground is quite uncertain and one of the main reasons that BT09 concentrated on nearby IRDCs. Poor understanding of the foreground emission is likely to limit the reliability of the mass surface densities and masses of IRDCs derived for large samples of objects (e.g. Simon et al. 2006; Peretto & Fuller 2009), especially for the more distant objects. Local heating of small dust grains that then produce MIR foreground emission cannot be accounted for in the BT09 model of foreground estimation and this can affect even nearby IRDCs. However, choosing relatively quiescent IRDCs can help minimize this particular source of uncertainty. One of the main goals of this paper is to introduce a new, improved method to measure the intensity of the foreground emission.

The structure of this paper is as follows. In §2 we introduce the method of saturation-based MIR extinction mapping. In §3 we present the results of applying this method to study the structure of 42 massive starless and

early-stage core/clumps located in 10 IRDCs. In §4 we discuss the implications of these results for massive star and star cluster formation theories.

2. SATURATION-BASED MIR EXTINCTION MAPPING

The MIREX mapping technique requires knowing the intensity of radiation directed towards the observer at a location just behind the cloud of interest, $I_{\nu,0}$, and just in front of the cloud, $I_{\nu,1}$. Then for negligible emission in the cloud and a simplified 1D geometry,

$$I_{\nu,1} = e^{-\tau_\nu} I_{\nu,0}, \quad (2)$$

where the optical depth $\tau_\nu = \kappa_\nu \Sigma$, where κ_ν is the total opacity at frequency ν per unit gas mass and Σ is the gas mass surface density.

We cannot see $I_{\nu,0}$ directly, so it must be estimated by interpolation from surrounding regions. BT09 tried two main ways to do this using median filters. The Large-Scale Median Filter (LMF) method used a square filter of size $13'$ that was much larger than the IRDCs of interest so that the clouds did not significantly depress the estimated median intensity. This has the advantage of not assuming any prior knowledge about the IRDC, but the disadvantage of a coarse angular resolution of background intensity fluctuations. For studying specific IRDCs that can be defined as occupying a certain region of the sky, e.g. an ellipse, we thus introduced the Small-Scale Median Filter (SMF) method. Here the size of the filter is set to be one-third of the major axis of the IRDC ellipse (defined by Simon et al. 2006), but it is only applied for background estimation outside of the IRDC ellipse. Inside the ellipse we estimate the background by interpolating from the surrounding background model. BT09 estimated that the uncertainties in background estimation due to this interpolation were at a level of $\lesssim 10\%$, which corresponds to $\Sigma \lesssim 0.013 \text{ g cm}^{-2}$.

However, because of foreground emission towards the IRDC, we actually observe (see Figure 1)

$$I_{\nu,1,\text{obs}} = I_{\nu,\text{fore}} + I_{\nu,1} = I_{\nu,\text{fore}} + e^{-\tau_\nu} I_{\nu,0}, \quad (3)$$

and towards the IRDC surroundings, where we are trying to estimate $I_{\nu,0}$, we actually observe

$$I_{\nu,0,\text{obs}} = I_{\nu,\text{fore}} + I_{\nu,0}. \quad (4)$$

The primary uncertainty in the MIREX mapping method of BT09 for larger values of Σ is the estimate of the level of the foreground contribution to the intensity, $I_{\nu,\text{fore}}$. In order to increase the method's sensitivity to higher values of mass surface density, we now describe a new, empirical method to estimate this contribution.

If a core has a high enough mass surface density, then it will block essentially all the background emission. The observed minimum intensity in the cloud will then be approximately equal to the foreground emission and the angular distribution of this intensity may appear to flatten or “saturate”. It is difficult to be certain if an individual dense core is saturated (as is sometimes assumed if the foreground is simply estimated from the darkest pixel, e.g. Ragan et al. 2009). However, we propose that if the minimum intensity is observed to “be the same” in two or more “independent” cores (i.e. spatially resolved peaks in Σ) in the same cloud, then this is very likely due to saturation. In practice, by “be the same” we adopt the condition to be within 2σ of each other, where σ is the uncertainty in the GLIMPSE $8 \mu\text{m}$ intensities of 0.6 MJy sr^{-1} (Reach et al. 2006). By “independent” we adopt an angular separation of at least $8''$ i.e. much larger than the $2''$ FWHM of the Spitzer IRAC $8 \mu\text{m}$ PSF.

The algorithm for this method is as follows (see also Figure 1):

- 1) Define a region of the sky as the “IRDC”. Following BT09, we use the ellipses from the catalog of Simon et al. (2006), which were based on MSX images.
- 2) Using GLIMPSE $8 \mu\text{m}$ images, find the minimum value of $I_{\nu,1,\text{obs}}$ inside the IRDC, $I_{\nu,1,\text{obs}}(\text{min})$.
- 3) Search for all pixels in the IRDC with $I_{\nu,1,\text{obs}}(\text{min}) < I_{\nu,1,\text{obs}} < I_{\nu,1,\text{obs}}(\text{min}) + 2\sigma$. If there are pixels meeting this criteria that are independent (to be conservative we adopt $\geq 8''$ away from the IRDC minimum), then the IRDC is defined to be saturated, all the above pixels are labeled as “saturated pixels”, and the following steps are carried out.
- 4) The mean value of $I_{\nu,1,\text{obs}}$ of the saturated pixels is evaluated, $I_{\nu,1,\text{obs}}(\text{sat})$. We set the foreground intensity (which includes all sources of emission: Galactic, Zodiacal and instrumental, Battersby et al. 2010) to be $I_{\nu,\text{fore}} = I_{\nu,1,\text{obs}}(\text{sat}) - 2\sigma$. This subtraction is motivated to have $I_{\nu,\text{fore}} < I_{\nu,1,\text{obs}}(\text{min})$ and thus give every pixel a finite value of τ and thus Σ .

If all the “saturated pixels”, defined above, really did have negligible values of $I_{\nu,1}$ and had a distribution of intensities that was relatively uniform in the above range, then $I_{\nu,\text{fore}} \simeq I_{\nu,0,\text{obs}}(\text{min}) + 1\sigma$ and our method would be underestimating $I_{\nu,\text{fore}}$ by $2\sigma = 1.2 \text{ MJy/sr}$. In fact, we do find for the ~ 300 “saturated pixels” in the 10 IRDCs of our sample, a mean value of $I_{\nu,1,\text{obs}} - I_{\nu,1,\text{obs}}(\text{min}) \simeq 0.7 \text{ MJy/sr}$. Thus, we are likely to be underestimating $I_{\nu,\text{fore}}$ (overestimating $I_{\nu,1}$) by an amount $\simeq 2\sigma = 1.2 \text{ MJy/sr}$. This leads to a value of Σ where our measured values are significantly affected by saturation:

$$\Sigma(\text{sat}) = \frac{\tau_\nu(\text{sat})}{\kappa_\nu} = \frac{\ln(I_{\nu,0}/I_{\nu,1})}{\kappa_\nu}, \quad (5)$$

where $I_{\nu,1}/I_{\nu,0} = I_{8\mu\text{m},1}/I_{8\mu\text{m},0} = e^{-\tau_{8\mu\text{m}}(\text{sat})}$ so $\tau_{8\mu\text{m}}(\text{sat}) = \ln(I_{\nu,0}/I_{\nu,1})$, that is set by $I_{\nu,1} = 2\sigma \rightarrow 1.2 \text{ MJy/sr}$. For a typical IRDC with $I_{\nu,0,\text{obs}} = 100 \text{ MJy/sr}$, $I_{\nu,\text{fore}} = f_{\text{fore}} I_{\nu,0,\text{obs}} = 30 \text{ MJy/sr}$ so that $I_{\nu,0} = 70 \text{ MJy/sr}$, then $\tau_{8\mu\text{m}}(\text{sat}) = 4.07$ and $\Sigma(\text{sat}) = 0.544 \text{ g cm}^{-2}$. For a region of such a cloud with a true value of $\Sigma = 0.5 \text{ g cm}^{-2}$ so that $I_{\nu,1} = 1.65 \text{ MJy/sr}$, if we have underestimated $I_{\nu,\text{fore}}$ by 1.2 MJy/sr , then we would infer $\Sigma = 0.427 \text{ g cm}^{-2}$. Similarly,

for a true $\Sigma = 0.4 \text{ g cm}^{-2}$, we would infer $\Sigma = 0.361 \text{ g cm}^{-2}$. The values of $\Sigma(\text{sat})$ calculated with $I_{8\mu\text{m},1} = 1.2 \text{ MJy/sr}$ for the 10 IRDCs in our sample are listed in Table 1. They range from $\Sigma(\text{sat})=0.33$ to 0.52 g cm^{-2} as one progresses along the Galactic plane towards $l = 0$, where the background is brightest.

An additional uncertainty results from our use of a single effective value of $\kappa_{8\mu\text{m}} = 7.5 \text{ cm}^2 \text{ g}^{-1}$ averaged over the *Spitzer* IRAC $8\mu\text{m}$ band, weighting by the filter response function, the spectrum of the Galactic background and the dust opacity model (BT09). Since these functions vary over this wavelength range (see Fig. 1 of BT09), at large optical depths the actual transmitted intensity will be greater than that predicted, being more dominated by the region of the spectrum with the lowest opacity. The net effect is an underestimation of the true mass surface density, given the observed ratio of transmitted to incident intensities. We have investigated the size of this effect by integrating the transfer equation (2) over the above weighting functions (see Fig. 2). For our fiducial dust model (the moderately coagulated thin ice mantle model of OH94), which has a relatively flat MIR opacity law, the effect is small: just a few percent effect up to value of $\Sigma \sim 1 \text{ g cm}^{-2}$, rising to about a 10% effect by $\Sigma = 10 \text{ g cm}^{-2}$. For illustrative purposes, Fig. 2 also shows the results for the Draine (2003) $R_V = 3.1$ dust model, more appropriate for the diffuse ISM, which has bare grains and stronger variation of opacity across this wavelength range. Now the effect leads to an underestimation of Σ by up to several tens of percent for $\Sigma \sim 1 \text{ g cm}^{-2}$. Other dust models we have considered, such as the Draine (2003) $R_V = 5.5$ model, have somewhat smaller underestimation factors.

A further additional systematic uncertainty results from the fact that the foreground intensity will vary across the IRDC, especially due to local radiation sources. The accuracy of the Σ values will be higher in regions closer to the locations of saturated cores, where $I_{\nu,\text{fore}}$ has been estimated and in IRDCs with minimal local heating sources.

3. RESULTS

3.1. IRDC Properties

Following the above algorithm, we find that all 10 IRDCs of the BT09 sample exhibit the effects of saturation. In hindsight, this is not too surprising since these clouds were selected to have relatively high contrast against the background. The Σ maps of the clouds are shown in Figs. 3 and 4. The properties of these clouds are listed in Table 1, where we also compare their properties to those derived with the SMF method of BT09 with the analytic model of foreground estimation. Using the saturation-based estimate of foreground emission, we find $I_{\nu,\text{fore}}$ and thus f_{fore} has increased in all the clouds. Thus the highest values of Σ that we infer have risen from $\sim 0.1 - 0.3 \text{ g cm}^{-2}$ in BT09 to $\sim 0.4 - 0.6 \text{ g cm}^{-2}$ in this paper. The mean values, $\bar{\Sigma}_{\text{SMF}}$ rise by smaller factors, so that the total cloud masses rise by on average a factor of 2.0. A comparison of the global properties of these IRDC with the predictions of theoretical models of the interstellar medium will be presented in a separate paper.

3.2. Massive Starless Cores and Clumps

3.2.1. Locating the Cores

The cores we are considering are a subset of those originally identified by Rathborne et al. (2006) based on their mm dust continuum emission, observed with the IRAM-30m Telescope at $11''$ FWHM angular resolution. BT09 selected 43 cores from the Rathborne et al. sample, excluding those with significant $8\mu\text{m}$ emission and those with low-contrast against the MIR background (i.e. with $\Sigma \lesssim 0.02 \text{ g cm}^{-2}$). Here, we have excluded one of the BT09 cores, E4, because its GLIMPSE image suffers from a diagonal boundary artifact where the intensity of the diffuse emission changes abruptly.

BT09 treated the cores as circular with radii equal to half the reported FWHM diameter of Gaussian fits that Rathborne et al. (2006) fitted to their mm continuum images. These circles were centered at the coordinates estimated by Rathborne et al. As discussed in §3.1, we expect our derived values of Σ to be higher (and more accurate) than those of BT09. Comparing the core masses of BT09 with those derived here for the same regions, we find they have typically increased by a factor of about 2.2.

In this paper, we now redefine the core center to be the center of the highest Σ pixel inside the previous core boundary. If there are two or more adjacent saturated pixels at the core center, then their average position is used to define the center. In fact, 17 of the 42 cores exhibit saturation. Occasionally, after inspecting the $8\mu\text{m}$ GLIMPSE and $24\mu\text{m}$ MIPS GAL images, we note the presence of MIR sources near ($< 7.5''$) the core center. This occurs in 9 of the 42 cores (B2, C6, C8, D5, D6, D8, E2, E3, I1). In order to focus on massive starless and early-stage cores, we shift the center to a new, nearby ($\lesssim 3''$) Σ maximum to avoid any major sources of MIR emission within a radius of $7.5''$ of the new center. In several cases (C4, D4, F2, J1), the Σ map inside the Rathborne et al. core boundary does not exhibit a well-defined high Σ peak. In these cases we select a new core center as close as possible to the Rathborne et al. core: normally this is within a few arcseconds of the boundary, but for F2 it is about $10''$ outside.

Figure 5a shows the Σ map of core A1, extracted from the larger image of IRDC A, shown in Fig. 3a. Pixels suffering from saturation are marked with small white squares. The core center is marked with a cross. Similar images of all 42 cores are shown in Figs. 6 to 12.

We note that 5 of the IRDCs (B, E, G, H, J) only have one core that exhibits saturation. This is possible because the condition to determine if an IRDC is saturated is based on independent positions (separated by at least $8''$) having the same foreground intensity (to within 2σ), rather than requiring 2 cores to meet this condition. The 42 cores we have selected for analysis are not meant to be a complete census of all the dense regions in these IRDCs. For example, IRDC J only has one core selected.

The core Σ maps exhibit complex structure. It is not easy to define the boundary of a core from its surrounding clump, especially when one recalls we are viewing a 3D structure in projection. $^{13}\text{CO}(1-0)$ data exist for these IRDCs via the Galactic Ring Survey (Jackson et al. 2006), but with poor angular resolution ($\sim 46''$). Also, in the cores we expect CO to be highly depleted from the gas phase due to freeze-out onto dust grain surfaces. Widespread CO depletion has been observed in IRDC H by comparing our Σ map with C^{18}O emission observed with the IRAM-30m Telescope (Hernandez et al. 2011). Fontani et al. (2011) observed N_2H^+ , which does not freeze-out so readily as CO, from 4 of our cores (C1, F1, F2, G2), but again with relatively poor angular resolution ($> 10''$). Thus, given the lack of high angular resolution molecular line data for all the cores, here we present a uniform analysis of core structure, based only on the extinction maps.

For simplicity, we first make radial profiles of mean total mass surface density, which we refer to as Σ_{cl} since it includes contribution from the clump (see below), considering a series of annuli extending from the core center with width equal to 1 pixel, i.e. $1.2''$. Fractional overlap of pixels with these annuli are accounted for. ‘‘Holes’’ in the Σ maps due to MIR sources are treated as having a zero, i.e. negligible, value. In general, these sources do not significantly affect our characterization of core structure, at least in the inner $\sim 7.5''$, since we have chosen cores that are relatively free of strong sources (E3 is the worst affected, and is somewhat exceptional in this regard). Larger annuli are minimally affected by individual MIR sources, which cover only a small fraction of the area. We extend the radial profiles out to a maximum angular scale equal to that reported by Rathborne et al. (2006) based on mm dust emission, i.e. a radius equal to one FWHM of their fitted Gaussian profile. As we will see, this is generally larger than the scale over which the core can be considered to be a single monolithic object.

For Core A1, Figure 5b shows $\Sigma_{\text{cl}}(r)$ with blue open square symbols, plotted at the radii corresponding to the center of each annulus. The total enclosed mass, which we refer to as the clump mass $M_{\text{cl}}(r)$, is indicated by the blue long-dashed line.

3.2.2. Core and Clump Properties at the $60 M_{\odot}$ Enclosed Mass Scale

Before considering a more detailed analysis of the radial structure, it is instructive to first consider the properties of these core/clump objects at a scale where the total mass enclosed is $M_{\text{cl}} = 60 M_{\odot}$. If all this mass were in a core, then such a core has the potential to form a $\sim 30 M_{\odot}$ star, given expected star formation efficiencies of $\sim 50\%$ due to protostellar outflows (Tan & McKee, in prep.). Note that there is of course no guarantee that all our sources will collapse in this way and on statistical grounds one would not expect them to: most are likely to undergo fragmentation to form lower-mass stars.¹ For Core A1, $60 M_{\odot}$ is enclosed within $R_{\text{cl}} = 0.0962$ pc, so at this scale $\bar{\Sigma}_{\text{cl}} = 0.431 \text{ g cm}^{-2}$. A black dashed circle with this radius is shown in Fig. 5a and these core properties are listed in Table 2. Core A1 happens to be one of the most extensively saturated cores at the scale of an enclosed mass of $60 M_{\odot}$ (along with C2, H1, I1, I2, J1), so these numbers are likely to be significantly affected by saturation (which causes us to underestimate Σ), so actually the radius enclosing $60 M_{\odot}$ would be smaller and $\bar{\Sigma}$ larger.

The distributions of the radii, R_{cl} , and mean mass surface densities, $\bar{\Sigma}_{\text{cl}}$, of the 42 core/clumps at the $M_{\text{cl}} = 60 M_{\odot}$ scale are shown in Figure 13a (with the 6 highly saturated cores — A1, C2, H1, I1, I2, J1 — shown as a shaded subset). The mean/median/RMS dispersion-about-the-mean of $R_{\text{cl}}(M_{\text{cl}} = 60 M_{\odot}) = 0.121/0.114/0.0238$ pc. The mean/median/RMS dispersion values of $\bar{\Sigma}_{\text{cl}}(M_{\text{cl}} = 60 M_{\odot}) = 0.296/0.318/0.0952 \text{ g cm}^{-2}$ (see also Table 3).

We next fit a power law density distribution,

$$\rho_{\text{cl}}(r) = \rho_{\text{s,cl}} \left(\frac{r}{R_{\text{cl}}} \right)^{-k_{\rho,\text{cl}}}, \quad (6)$$

where $\rho_{\text{s,cl}} = \mu_{\text{H}} n_{\text{H,s,cl}}$ (with $\mu_{\text{H}} = 2.34 \times 10^{-24} \text{ g}$) is the density at the surface of the clump, R_{cl} . We project the above distribution to derive $\Sigma_{\text{cl}}(r)$, which we then convolve with a Gaussian with a FWHM of $2''$ (to allow for the *Spitzer* IRAC $8 \mu\text{m}$ PSF). We then fit this model to the observed $\Sigma_{\text{cl}}(r)$ profile, excluding annuli that are significantly ($> 50\%$) affected by saturated pixels. For Core A1, $k_{\rho,\text{cl}} = 1.40$ and $n_{\text{H,s,cl}} = 2.47 \times 10^5 \text{ cm}^{-3}$. For the whole sample, the mean/median/dispersion values of $k_{\rho,\text{cl}} = 1.09/1.10/0.236$ and $n_{\text{H,s,cl}} = (1.76/1.85/0.852) \times 10^5 \text{ cm}^{-3}$. These distributions are shown in Fig. 13a with the blue dotted histograms. The values for individual cores are listed in Table 2.

The above analysis is somewhat simplistic in that it has assumed the structure exists in isolation. In reality, we see that these high Σ objects are surrounded by regions that also have significant mass surface densities. Thus next we model the cores with a similar power law density structure,

$$\rho_{\text{c}}(r) = \rho_{\text{s,c}} \left(\frac{r}{R_{\text{c}}} \right)^{-k_{\rho,\text{c}}}, \quad (7)$$

but now when comparing to the observed Σ maps we account for the mass surface density of the surrounding clump medium, $\Sigma_{\text{cl,env}}$. We estimate $\Sigma_{\text{cl,env}}$ using the observed value in the annular region from R_{c} to $2R_{\text{c}}$. This choice is motivated by the desire to sample a region of the clump that has a scale comparable to the core in both size and

¹ One cannot distinguish between massive star formation Core Accretion and Competitive Accretion theories (Bonnell et al. 2001) simply by observing that a massive structure is actually composed of sub-fragments (c.f. Bontemps et al. 2010, their section 4.6).

mass². We assume this same value of $\Sigma_{\text{cl,env}}$ covers the area of the core, and so subtract it from the interior $\Sigma_{\text{cl}}(r)$ profile to derive the mass surface density profile of the core, $\Sigma_c(r)$. Thus note that $\Sigma_{\text{cl,env}} = \bar{\Sigma}_{\text{cl}} - \bar{\Sigma}_c$.

For the same $M_{\text{cl}} = 60 M_\odot$ enclosed mass scale as defined above, we set $R_c = R_{\text{cl}}(M_{\text{cl}} = 60 M_\odot)$. The masses contained in the cores, based on integrating the $\Sigma_c(r)$ profile, are of course less than the $60 M_\odot$ we previously identified with the clump. For Core A1, we derive a core mass of $M_c = 37.9 M_\odot$ with $\bar{\Sigma}_c = 0.316 \text{ g cm}^{-2}$. Its value of $k_{\rho,c} = 2.04$ and $n_{\text{H,s,c}} = 1.21 \times 10^5 \text{ cm}^{-3}$, i.e. a steeper density profile with a lower value of the volume density at the surface than was derived previously. For the 42 cores we find the mean/median/dispersion values of $M_c = 30.4/30.4/12.7 M_\odot$, $\bar{\Sigma}_c = 0.139/0.160/0.0738 \text{ g cm}^{-2}$, $k_{\rho,c} = 1.64/1.67/0.271$ and $n_{\text{H,s,c}} = (0.639/0.750/0.394) \times 10^5 \text{ cm}^{-3}$ (See red solid line histograms in Fig. 13a and Tables 2 & 3). Compared to the clump results (i.e. derived from the total Σ profiles), above, for the envelope-subtracted core properties we necessarily find smaller surface densities, steeper density profiles and smaller volume densities.

The power law fits ignore annuli affected by significant saturation, where Σ is underestimated. Thus we also estimate a core mass, $M_{c,\text{PL}}$, based on extrapolation of the power law fits to the center of the core:

$$M_{c,\text{PL}} = \frac{4\pi}{3 - k_{\rho,c}} \rho_s R_c^3 = \frac{43.5}{3 - k_{\rho,c}} \frac{n_{\text{H,s,c}}}{10^5 \text{ cm}^{-3}} \left(\frac{R_c}{0.1 \text{ pc}} \right)^3 M_\odot \quad (k_{\rho,c} < 3) \quad (8)$$

There are no cores where the derived $k_\rho > 3$ for which the inner boundary condition would have been considered. If there were, then in these cases we would expect to truncate the power law at the Jeans scale in the core. For Core A1, $M_{c,\text{PL}} = 49.2 M_\odot$, about 30% times larger than M_c . Such an increase is expected since this is one of the most extensively saturated cores. For the rest of the 42 cores the change is typically much smaller. The mean/median/dispersion values of $M_{c,\text{PL}} = 31.1/31.0/13.5 M_\odot$ and $\bar{\Sigma}_{c,\text{PL}} = 0.154/0.171/0.0899$ (See red solid line histograms in Fig. 13a and Tables 2 & 3).

3.2.3. Best-fit Power Law Cores

We now repeat the power law core plus clump envelope fitting procedure as a function of radius, starting at the inner region with 3 unsaturated annuli for the core. An annulus twice as large in radius is used to estimate the value of Σ of the clump envelope, $\Sigma_{\text{cl,env}}$. We assess the relative goodness of fit of this model as a function of r by finding the minimum of the reduced χ^2 parameter, defined by

$$\chi^2 \equiv \sum_{i=1,N} \frac{1}{\nu} \frac{[\Sigma_{c,\text{PL}}(r) - \Sigma_{c,i}(r)]^2}{\sigma_i^2} \quad (9)$$

where N is the number of annuli, $\nu = N - 2$ is the number of degrees of freedom and σ is the error for each annulus, which we take to be $\sigma = 0.01 \text{ g cm}^{-2} + 0.2 \Sigma_c$. Note, that because of the $2''$ angular resolution of *Spitzer* IRAC, adjacent annuli are not completely independent. However, the relative values of χ^2 should still give a measure of the best-fitting model.

We place some additional constraints on the fitting. First, we do not allow the best-fit core to extend beyond neighboring core centers (from our sample of 42 cores). Second, to prevent independent discrete structures that are not part of our core sample from influencing the fitting, we check for a 3σ rise in the Σ_c profile by comparing the annulus before any rise begins to the following local maximum. If this occurs, we ignore fits beyond the pre-rise annulus, and search inward for a local maximum in χ_ν^2 and define that to be the best-fit radius (for example, this occurs in Core A3). Third, if more than 25% of an annulus is composed of MIR emission pixels, we do not extend the fit any further. In these cases, a prior unaffected annulus with a local maximum in χ_ν^2 is chosen as the best-fit radius (this circumstance only arises in Core E3). As a result of the above constraints, it is possible that the global minimum of χ_ν^2 will not be chosen as the “best-fit”.

The results for $M_c(r)$, $k_{\rho,c}(r)$ and $-\log \chi^2(r)$ are shown for Core A1 in Fig. 5b. The location of the peak value of $-\chi^2$ indicates the best-fitting power law (PL) core radius, which occurs at 0.251 pc with a value of $\chi^2 = 1.62$. A circle of this best-fit core radius is shown in the Σ map of the core in Fig. 5a. The total enclosed mass at this scale is $M_{\text{cl}} = 303 M_\odot$, the core mass is $M_c = 194 M_\odot$, the mean core mass surface density is $\bar{\Sigma}_c = 0.204 \text{ g cm}^{-2}$ and the clump surrounding the core has $\Sigma_{\text{cl,env}} = \bar{\Sigma}_{\text{cl}} - \bar{\Sigma}_c = 0.115 \text{ g cm}^{-2}$. The core mass based on integrating the power law profile is $M_{c,\text{PL}} = 204 M_\odot$, yielding a slightly higher mean mass surface density of $\bar{\Sigma}_{c,\text{PL}} = 0.214 \text{ g cm}^{-2}$.

The best-fit total $\Sigma_{\text{cl}}(r) = \Sigma_c(r) + \Sigma_{\text{cl,env}}$ model profile is shown by the solid line in Fig. 5b (the dotted continuation in the inner region indicates where annuli affected by saturation are not used in the fitting). Figure 5c shows the clump envelope subtracted profile of $\Sigma_c(r)$, together with various projected power law fits, including the best-fit value of $k_{\rho,c} = 1.88$. The parameters of the best-fitting power law plus clump envelope model are listed in Table 2.

The distributions of R_c , $\bar{\Sigma}_{\text{cl}}$ (which is the mean total Σ over the area of the core), $\bar{\Sigma}_{c,\text{PL}}$, $k_{\rho,\text{cl}}$, $k_{\rho,c}$, $n_{\text{H,s,cl}}$, $n_{\text{H,s,c}}$, M_{cl} and $M_{c,\text{PL}}$ are shown in Figure 13b and summarized in Table 3. The values for each core are listed in Table 2.

It is important to note that these “best-fit” values may not necessarily be the most accurate description of the core structures. They are based on azimuthally-averaged quantities. The Σ map of a particular core should be inspected

² We have also tried measuring $\Sigma_{\text{cl,env}}$ from a thin, $1.2''$ wide annulus just outside R_c , which generally leads to larger estimated values of $\Sigma_{\text{cl,env}}$. However, we consider that this thin-shell annulus does not sample a large enough region and mass of the clump that, via self-gravity, would be responsible for setting core’s surrounding pressure (see discussion in §1).

to gauge the validity of this assumption. Also, the values of χ^2 as a function of radius should be checked to gauge the reasonableness and uniqueness of the fit.

The radii and masses of the best-fit cores are generally, but not always, larger than those at the $M_{\text{cl}} = 60 M_{\odot}$ scale, and thus the volume densities are generally lower. The mean/median/dispersion values of $k_{\rho,\text{cl}} = 1.10/1.12/0.246$ and $k_{\rho,c} = 1.58/1.56/0.277$ are however very similar to those derived at the $M_{\text{cl}} = 60 M_{\odot}$ scale, which suggests that the assumption by McKee & Tan (2002) and MT03 of a self-similar hierarchy of structure from the clumps to core scales is a reasonable one. The fiducial value they adopted of $k_{\rho} = 1.5$ also is close to the average values found in this sample. In Figure 14 we plot $k_{\rho,c}$ versus $M_{c,\text{PL}}$, $\bar{\Sigma}_{c,\text{PL}}$ and $\Sigma_{\text{cl,env}}$ for the best-fit cores. There are no apparent correlations of $k_{\rho,c}$ with these properties.

3.2.4. Best-fit Bonnor-Ebert Cores

We perform a similar analysis as the power law plus constant envelope fitting as a function of radius, but now using critical Bonnor-Ebert profiles (varying the total effective sound speed, c_s and surface pressure, P_0) plus a constant envelope. See Dapp & Basu (2009) for more details about fitting Bonnor-Ebert profiles to column density data.

The best-fitting model for Core A1 is shown in Fig. 5d. This has $R_c = 0.670$ pc, $M_c = 353 M_{\odot}$, $\bar{\Sigma}_c = 0.0523 \text{ g cm}^{-2}$, $c_s = 0.275 \text{ km s}^{-1}$ and $P_0/k = 8.9 \times 10^7 \text{ K cm}^{-3}$. However, the value of $\chi^2 = 8.75$, which is significantly larger, i.e. worse, than the best-fit power law plus clump envelope model fit (for which $\chi^2 = 1.62$). Also the size of the Bonnor-Ebert fitted core is much larger than the power law model: as can be seen from Fig. 5a, on these larger scales the assumption of single monolithic and azimuthally symmetric structure becomes less valid.

Carrying out the Bonnor-Ebert analysis for all 42 cores, we find the fits are generally worse than for the power law models. The best-fitting Bonnor-Ebert radii are typically larger than those of the power law core models. For these reasons, we do not consider the Bonnor-Ebert models further in our discussion.

4. DISCUSSION & CONCLUSIONS

We have presented a new method to accurately probe mass surface densities in the range ~ 0.01 to $\sim 0.5 \text{ g cm}^{-2}$ on arcsecond scales in quiescent, infrared dark clouds, some of which are likely to be the sites of future star formation. The method uses the small-scale median filter method of background interpolation from regions around a defined IRDC (BT09) and then estimates the level of foreground emission by seeing if there are *independent, nearby, saturated cores* within the IRDC. If so, the foreground level is set equal to that observed towards these saturated regions. The resulting Σ measurements derived from this MIREX mapping depend on the assumed MIR dust opacity per unit total mass, but do not depend on the dust temperature, which is a distinct advantage over measurements based on sub-mm/mm dust continuum emission.

Focusing on 42 core/clumps within 10 IRDCs, we have tried various methods of characterizing their azimuthally-averaged structure. Our preferred method, following the model of McKee & Tan (2002, 2003), involves fitting power law cores surrounded by a clump envelope, which is assumed to have a constant value of Σ that can be estimated from the surrounding region. We have fitted these models as a function of radius from the core center, deriving an overall best-fit, but also presenting the full results of this radial characterization. The typical value of the volume density power law index that best describes the cores is $k_{\rho,c} \simeq 1.6$. This is close to the fiducial value of 1.5 adopted by McKee & Tan (2002, 2003), who based their choice on previous measurements on the larger, \sim parsec, scales of gas clumps. We find this power law index does not appear to vary significantly with scale (i.e. between the $60 M_{\odot}$ enclosed mass scale and the best-fit power law plus clump scale), nor with other core or clump properties, suggesting the presence of a self-similar hierarchy of structure.

On the scale at which the total projected enclosed mass is $60 M_{\odot}$, the derived cores have about 50% of this mass. If massive star formation is to occur, then this is the material that has a high probability of being incorporated into the massive star. These cores have typical radii of $\simeq 0.1$ pc, masses of $\sim 30 M_{\odot}$, mean mass surface densities of $\bar{\Sigma}_c \simeq 0.15 \text{ g cm}^{-2}$ and surrounding clump mass surface densities of similar values. If one regards our method of clump envelope subtraction to be an overestimate, then one can consider the typical properties of the clumps on these scales as being representative of the gas that will form massive stars, i.e., with $M_{\text{cl}} = 60 M_{\odot}$ and $\Sigma_{\text{cl}} \simeq 0.3 \text{ g cm}^{-2}$.

The above values of Σ_{cl} are lower by factors of $\sim 3 - 7$ than the fiducial value of 1 g cm^{-2} considered by McKee & Tan (2002, 2003). Note, their theoretical model is general and does not require a particular value of Σ_{cl} , so this difference does not require any physical explanation. However, Krumholz & McKee (2008) have proposed massive star formation requires $\Sigma_{\text{cl}} \gtrsim 1 \text{ g cm}^{-2}$, based on a model in which fragmentation of massive cores is prevented by radiative heating from surrounding lower-mass protostars. The high value of Σ_{cl} is required so that the lower-mass protostars accrete at high enough rates that they are luminous enough to sufficiently heat the massive core.

Since massive star formation occurs relatively rarely, it may be that it occurs preferentially in cores with higher values of Σ_c and Σ_{cl} than we have observed for the average of our sample, which we note does show significant dispersion. However, we consider this unlikely given that we have selected the highest Σ regions from 10 IRDCs that show some of the highest contrast against the Galactic MIR background (selected from the larger sample of 38 IRDCs studied by Rathborne et al. 2006).

Saturation limits our Σ maps to values of $\simeq 0.5 \text{ g cm}^{-2}$ and this may be affecting our ability to find the highest Σ cores. However, we are excluding the saturated regions when deriving core and clump density profiles and most cores do not exhibit extensively saturated centers. We expect our choice of MIR opacity per unit gas mass may be uncertain by $\sim 30\%$ (see §1), so this by itself is unlikely to explain the relatively low values of Σ that we are deriving compared to the Krumholz & McKee (2008) prediction.

Another possibility, is that these cores and clumps will evolve to higher values of Σ before massive star formation occurs. Indeed, the fact that these are IR dark objects suggests that they cannot yet be experiencing much radiative heating. However, there is observational evidence for star formation activity in some of these cores. For example, Y. Wang et al. (2006) observed water maser emission located $4.31''$ from the center of Core C1. K. Wang et al. (2011) have reported protostellar outflows from Core C2.

To better compare our IRDC core/clump sample with more evolved systems, in Figure 15 we show the 42 core/clumps on the Σ versus M diagram (following Tan 2007). Here, Σ is measured from the total observed mass inside a given radial distance from the core/clump center. In Figure 16 we compare these profiles to the properties of the 31 star-forming clumps whose IR and sub-mm dust continuum emission was observed and modeled by Mueller et al. (2002). Note that these properties depend on the (1D) modeled temperature structure, dust emissivity (they used the same Ossenkopf & Henning (1994) dust model that we have adopted for our MIREX maps) and gas-to-dust ratio (we have scaled Mueller et al.'s masses by a factor 1.56 to be consistent with our adopted gas-to-dust ratio).

The IRDC cores/clumps overlap only with the lower- Σ range of the star-forming core/clump sample, perhaps indicating there is a (physically plausible) evolutionary growth in core/clump density as star formation proceeds. However, note that many (indeed most) star-forming cores and clumps have $\Sigma < 1 \text{ g cm}^{-2}$. Alternatively, the lack of starless high Σ core/clumps may be due to the somewhat smaller volume of the Galaxy that we have probed with our nearby IRDC sample, compared to the Mueller et al. star-forming core/clump sample.

Mueller et al. (2002) found density power law indices of $k_{\rho, \text{cl}} = 1.8 \pm 0.4$, slightly steeper than our derived values for IRDC cores of $k_{\rho, c} \simeq 1.6$, but significantly steeper than our value for clumps of $k_{\rho, \text{cl}} \simeq 1.1$. Again, this latter difference may indicate an evolution in cloud properties as star formation proceeds.

Considering the above results, we suggest that the initial conditions of local massive star formation in the Galaxy may be better characterized with values of $\Sigma_{\text{cl}} \simeq 0.2 \text{ g cm}^{-2}$ rather than 1 g cm^{-2} , which would imply smaller accretion rates and longer formation times than the fiducial values of MT03. The accretion rate becomes

$$\dot{m}_* = 1.37 \times 10^{-4} \left(\frac{m_{*f}}{30 M_\odot} \right)^{3/4} \left(\frac{\Sigma_{\text{cl}}}{0.2 \text{ g cm}^{-2}} \right)^{3/4} \left(\frac{m_*}{m_{*f}} \right)^{0.5} M_\odot \text{ yr}^{-1} \quad (10)$$

for a core with $k_{\rho, c} = 1.5$ and a star formation efficiency of 50%, where m_* is the instantaneous protostellar mass and m_{*f} is the final protostellar mass. The star formation timescale becomes

$$t_{*f} = 4.31 \times 10^5 \left(\frac{m_{*f}}{30 M_\odot} \right)^{1/4} \left(\frac{\Sigma}{0.2 \text{ g cm}^{-2}} \right)^{-3/4} \text{ yr}. \quad (11)$$

In this case of massive star formation at relatively low values of Σ , we expect fragmentation of the cores is prevented by magnetic fields, i.e. if the core mass is equal to the magnetic critical mass (Bertoldi & McKee 1992)

$$M_B = 1020 \left(\frac{R}{Z} \right)^2 \left(\frac{\bar{B}}{30 \mu\text{G}} \right)^3 \left(\frac{\bar{n}_H}{10^3 \text{ cm}^{-3}} \right)^{-2} M_\odot, \quad (12)$$

where R and Z are the major and minor axes of the core, \bar{B} is the mean field strength in the core, and \bar{n}_H is the mean number density of H nuclei. Thus for a core with $\bar{n}_H = 10^5 \text{ cm}^{-3}$ and $M_c = 100 M_\odot$, typical of our sample, the condition $M_B = M_c$ requires a field strength

$$\bar{B} = 300 \left(\frac{M_B}{100 M_\odot} \right)^{1/3} \left(\frac{Z}{R} \right)^{2/3} \left(\frac{\bar{n}_H}{10^5 \text{ cm}^{-3}} \right)^{2/3} \mu\text{G}. \quad (13)$$

If cores have some significant magnetic support, then we expect $R/Z > 1$, perhaps ~ 2 , so that the required field strength in eq.(13) is then $190 \mu\text{G}$. Such field strengths are similar to those observed in regions of active massive star formation (e.g. Crutcher 2005). Indeed, Crutcher (2005) noted the observed mass to flux ratios scattered about the critical value. Numerical simulations of the collapse of marginally magnetically critical (rather than super critical, e.g. Wang et al. 2010; Hennebelle et al. 2011) cores are required to investigate this scenario for forming massive stars, and, more generally, for explaining the high-mass tail of the initial mass function (Kunz & Mouschovias 2009).

MJB acknowledges support from a Sigma Xi Grant in Aid of Research. JCT acknowledges support from NSF CAREER grant AST-0645412; NASA Astrophysics Theory and Fundamental Physics grant ATP09-0094; NASA Astrophysics Data Analysis Program ADAP10-0110 and a Faculty Enhancement Opportunity grant from the University of Florida. We thank Peter Barnes, Paola Caselli, Ed Churchwell, Francesco Fontani, Audra Hernandez, Jouni Kainulainen, Jens Kauffmann, Shuo Kong, Mark Krumholz, Chris McKee, Thushara Pillai, Sven Van Loo, Qizhou Zhang for helpful discussions.

REFERENCES

- Battersby, C., Bally, J., Jackson, J. M. et al. 2010, ApJ, 721, 222
- Bertoldi, F., & McKee, C. F. 1992, ApJ, 395, 140
- Beuther, H., Schilke, P., Menten, K.M., Motte, F., Sridharan, T.K., & Wyrowski, F. 2002, ApJ, 566, 945
- Bonnell, I. A., Clarke, C. J., Bate, M. R., & Pringle, J. E. 2001, MNRAS, 324, 573
- Bontemps S., Motte, F., Csengeri, T., Schneider, N., 2010, A&A, 524, A18
- Butler, M. J. & Tan, J. C., 2009, ApJ, 696, 484
- Crutcher, R. M. 2005, in *Massive star birth: A crossroads of Astrophysics*, IAU Symp. 227, ed. by Cesaroni, R., Felli, M., Churchwell, E., Walmsley, M., (Cambridge: CUP), pp.98
- Dapp, W.B., Basu, S. 2009, MNRAS, 395, 1092
- Draine, B. T., 2011, ApJ, 732, 100
- Egan, M. P., Shipman, R. F., Price, S. D., et al. 1998, ApJ, 494, L199
- Fontani, F., et al. 2011, A&A, 529, L7
- Hennebelle, P., Commerçon, B., Joos, M., et al. 2011, A&A, 528, 72
- Hernandez, A. K., Tan, J. C., 2011, ApJ, 730, 44
- Hernandez, A. K., Tan, J. C., Caselli, P., et al. 2011, ApJ, 738, 11
- Jackson, J. M., Rathborne, J. M., Shah, R. Y., et al. 2006, ApJS, 163, 145
- Kainulainen, J., Alves, J., Beuther, H., et al. 2011, A&A, 536, 48
- Kunz, M. W., & Mouschovias, T. Ch. 2009, MNRAS, 399, L94
- Krumholz, M. R., & McKee, C. F. 2008, Nature, 451, 1082
- Kurayama, T., Nakagawa, A., Sawada-Satoh, S. et al. 2011, PASJ, 63, 513
- McKee, C. F., Tan, J. C., 2002, Nature, 416, 59
- McKee, C. F., & Tan, J. C. 2003, ApJ, 585, 850 (MT03)
- Mueller, K. E., Shirley, Y. L., Evans, N. J., II, & Jacobson, H. R. 2002, ApJS, 143, 469
- Ossenkopf, V., & Henning, T. 1994, A&A, 291, 943
- Perault, M., et al. 1996, A&A, 315, L165
- Peretto, N., & Fuller, G. A. 2009, A&A 505, 405
- Rathborne, J. M., Jackson, J. M., & Simon, R. 2006, ApJ, 641, 389
- Reach, W. T., Rho, J., Tappe, A., et al. 2006, AJ, 131, 1479
- Shu, F. H., Adams, F.C., Lizano, S. 1987, ARA&A, 25, 23
- Simon, R., Jackson, J. M., Rathborne, J. M., Chambers, E. T. 2006, ApJ, 639, 227
- Tan, J. C., 2007, IAU Symp. 237, 258, Triggered Star Formation in a Turbulent ISM, Edited by B. G. Elmegreen and J. Palous, Cambridge University Press, p258
- Tan, J. C., 2008, in ASP Conf. Ser. 387, Massive Star Formation: Observations Confront Theory, eds. Beuther et al., p346
- van der Tak, F. F. S., van Dishoeck, E. F., Evans, N. J., II, Blake, G. A. 2000, ApJ, 537, 283
- Wang, K., Zhang, Q., Wu, Y., Zhang, H. 2011, ApJ, 735, 64
- Wang, P., Li, Z-Y., Abel, T., Nakamura, F. 2010, ApJ, 709, 27
- Wang, Y., Zhang, Q., Rathborne, J. M., Jackson, J., Wu, Y. 2006, ApJ, 651, L125

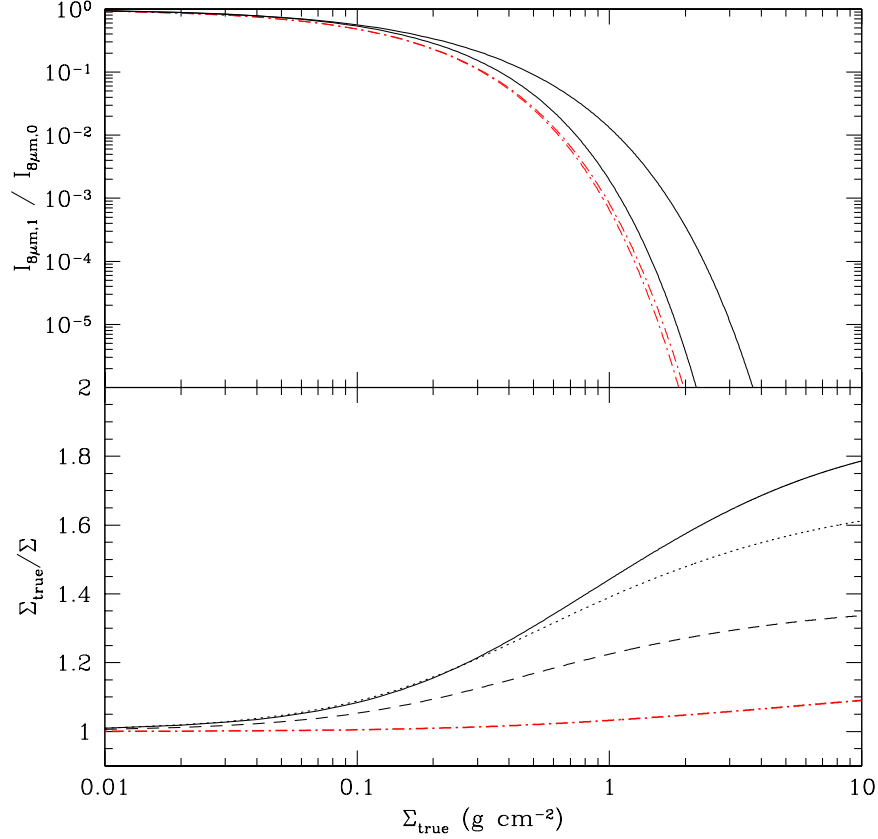


FIG. 2.— Effect of finite filter width on estimates of Σ and accuracy of an approximation using a single band-averaged opacity (see text). The *Spitzer* IRAC band 4, i.e. $8\mu\text{m}$, filter has sensitivity from about 6.5 to $9.5\mu\text{m}$. *Top panel:* Ratio of transmitted to incident flux as a function of true mass surface density, Σ_{true} . The result for the band-average opacity for the moderately coagulated thin ice mantle dust model of OH94 (our fiducial model) is shown by the lower red dot-dashed line. The actual transmitted flux, calculated by integrating the transfer equation over the bandpass, is shown by the upper red dot-dashed line. The equivalent quantities for the Draine (2003) $R_V = 3.1$ dust model are shown by the lower and upper black solid lines: the effect is larger here as this dust model shows larger opacity variations across the band. *Bottom panel:* Effect on estimation of Σ . Given an observed ratio of transmitted to incident intensities, the true mass surface density, Σ_{true} , will be greater than that estimated using the band-averaged opacity, Σ . The ratio of $\Sigma_{\text{true}}/\Sigma$ is shown by the red dot-dashed line for the above OH94 thin ice mantle model. The OH94 uncoagulated thin ice mantle model gives essentially the same result. The error is a few percent in the region of interest of the IRDC cores in this study. Also shown are these effects for the Draine (2003) $R_V = 3.1$ (black solid line), $R_V = 5.5$ (black dotted line) and $R_V = 5.5$ Case B (black dashed line).

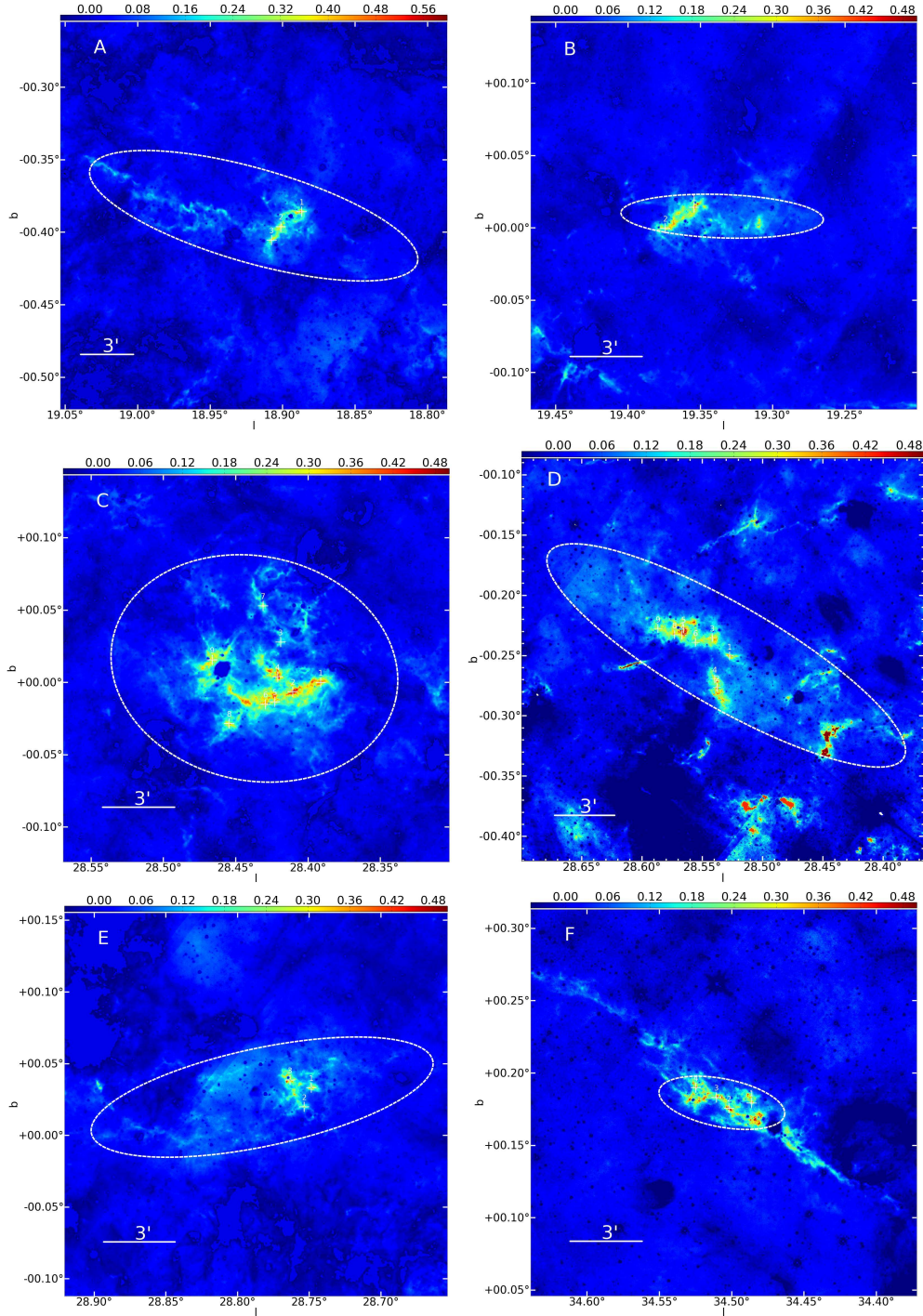


FIG. 3.— Mass surface density, Σ_{SMF} , maps of IRDCs A-F derived from MIREX mapping using *Spitzer* IRAC $8\ \mu\text{m}$ images with pixel scale of $1.2''$ and angular resolution of $2''$ using a saturation-based estimate of the foreground emission (§2). The color scale is indicated in g cm^{-2} . The dashed ellipse, defined by Simon et al. (2006) based on MSX images, defines the region where the background emission is estimated not directly from the small-scale median filter average of the image intensity, but rather by interpolation from nearby regions just outside the ellipse. The locations of the massive starless cores we have selected for analysis (§3) are marked with crosses. Bright MIR sources appear as artificial “holes” in the map, where we have set the values of $\Sigma = 0\ \text{g cm}^{-2}$.

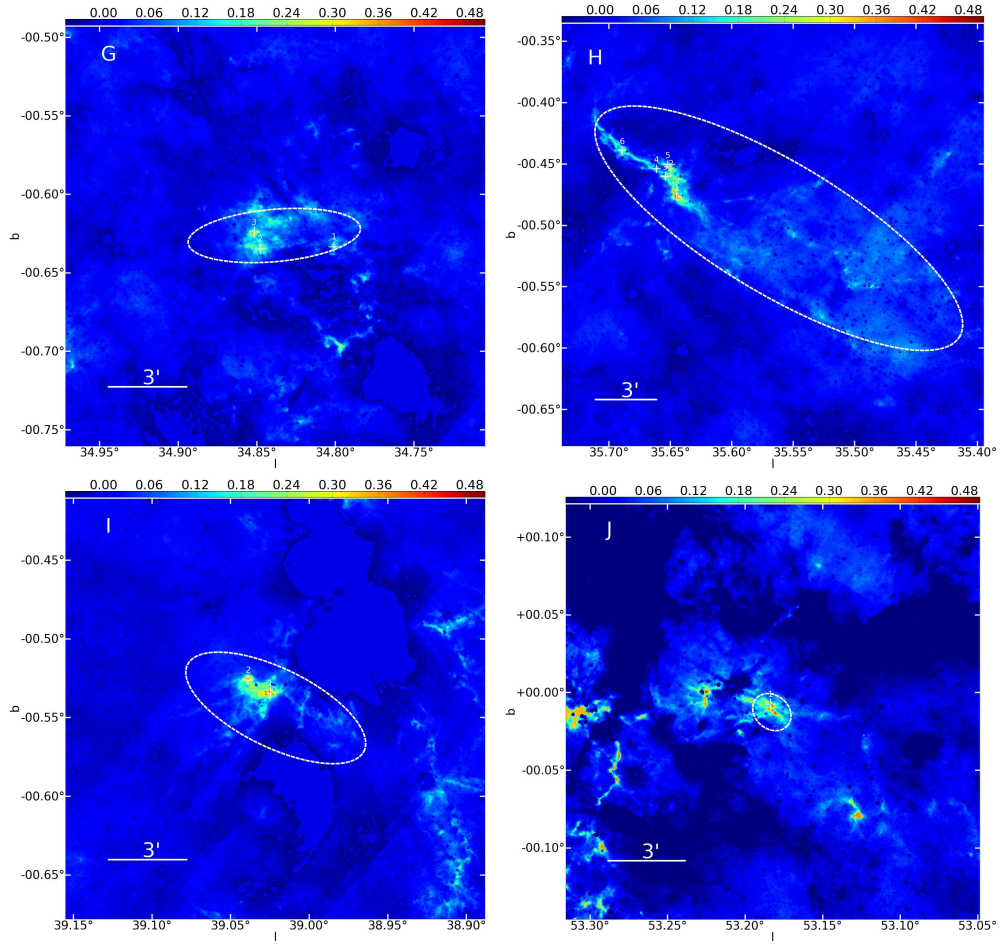


FIG. 4.— Mass surface density, Σ_{SMF} , maps (in the same format as Fig. 3) of IRDCs G-J derived from MIREX mapping using *Spitzer* IRAC $8\ \mu\text{m}$ images.

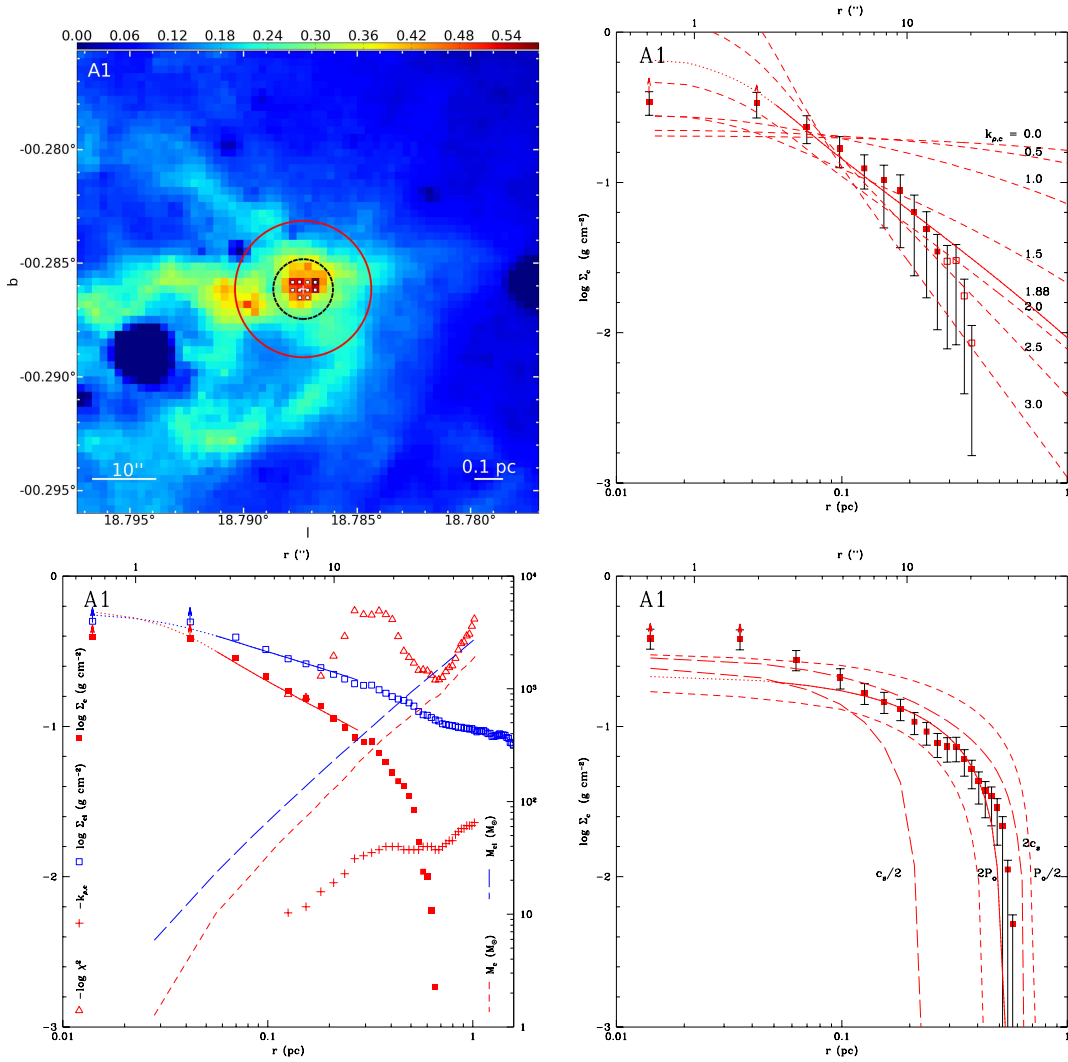


FIG. 5.— (a) *Top Left*: Mass surface density, Σ_{SMF} , map in g cm^{-2} of IRDC Core A1, extracted from the map of IRDC A (Fig. 3). The core center is marked with a cross. Saturated pixels, for which Σ is a lower-limit of the true value, are marked with small white squares. The black dashed circle shows the radius enclosing a total mass of $60 M_{\odot}$. The red solid circle shows the extent of the core derived from the best-fit power law (PL) core plus envelope model (see text). (b) *Bottom Left*: Radial profiles of Core A1: observed $\log \Sigma_{\text{cl}}/(\text{g cm}^{-2})$ (blue open squares, plotted at annuli centers) derived from the map shown in (a); total projected enclosed mass, M_{cl} , (blue long-dashed line [see right axis]); core mass, M_{c} after clump envelope subtraction (red dashed line [see right axis]); index of core PL density profile, $k_{\rho,c}$, (red crosses); $-\log \chi^2$ (red triangles) of the PL plus envelope fit (best-fit has a maximum or local maximum value [see text]); the best-fit PL plus envelope model (blue solid line; dotted line shows range affected by saturation that was not used in the fitting); $\log \Sigma_{\text{c}}/(\text{g cm}^{-2})$ of best-fit core after envelope subtraction (red solid squares) and PL fit (red solid line; dotted line shows range affected by saturation that was not used in the fitting). (c) *Top Right*: $\Sigma_{\text{c}}(r)$, i.e. after clump envelope subtraction for the best-fit model (red solid squares; open squares show residual, post-subtraction envelope material). PL models with various values of $k_{\rho,c}$ are indicated (dashed lines), including the best-fit model with $k_{\rho} = 1.88$ (solid line). (d) *Bottom Right*: As for (c) but for Bonnor-Ebert (BE) plus envelope fitting. $\Sigma_{\text{c}}(r)$, i.e. after clump envelope subtraction for the best-fit model (red solid squares). Best-fit BE model (solid line) and models varying c_{s} (long-dashed lines) and P_0 (dashed lines) by factors of 2 from this are shown (see text).

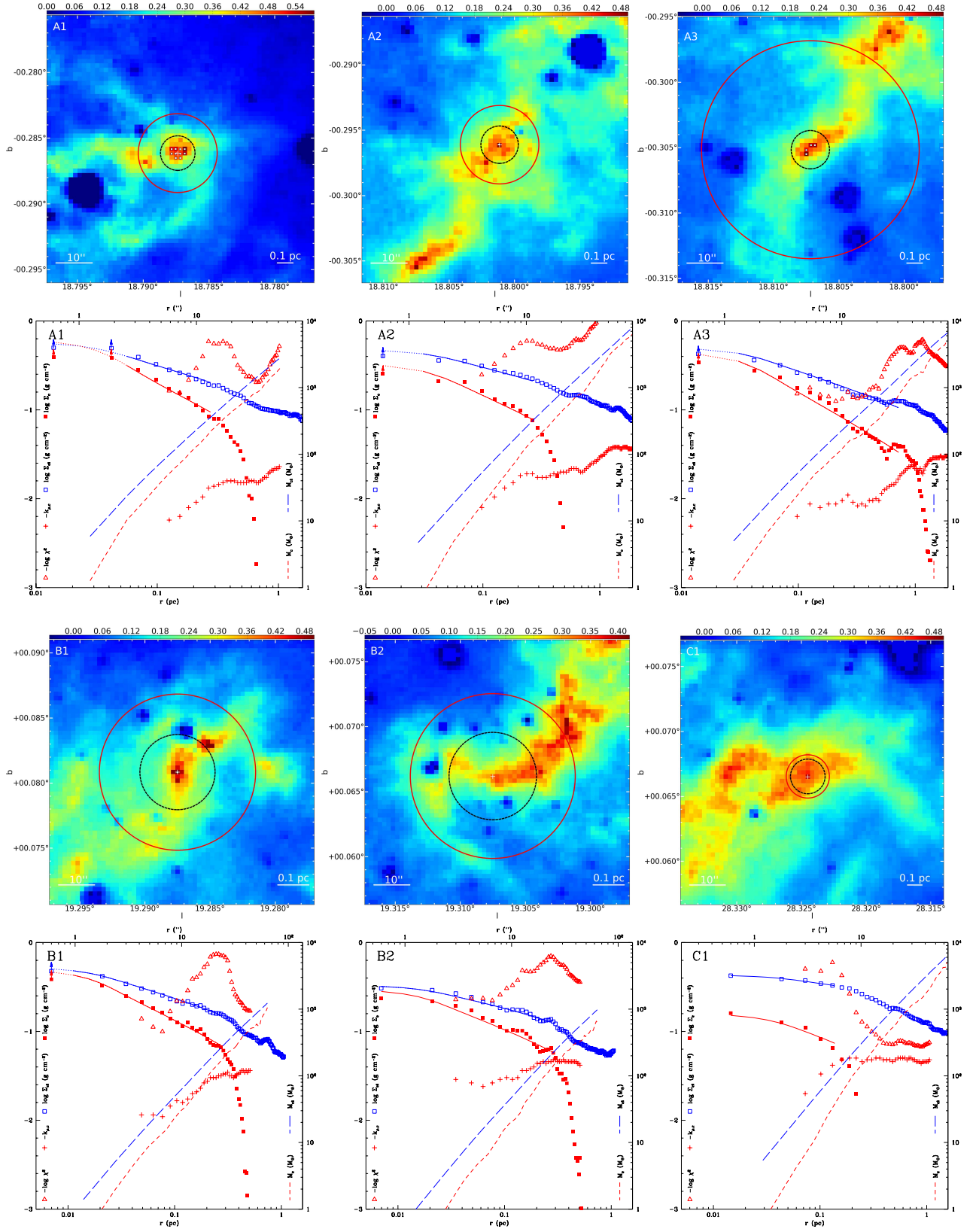


FIG. 6.— Core A1, A2, A3, B1, B2, C1 Σ maps (notation as Fig. 5a) and azimuthally averaged radial profile figures (notation as Fig. 5b).

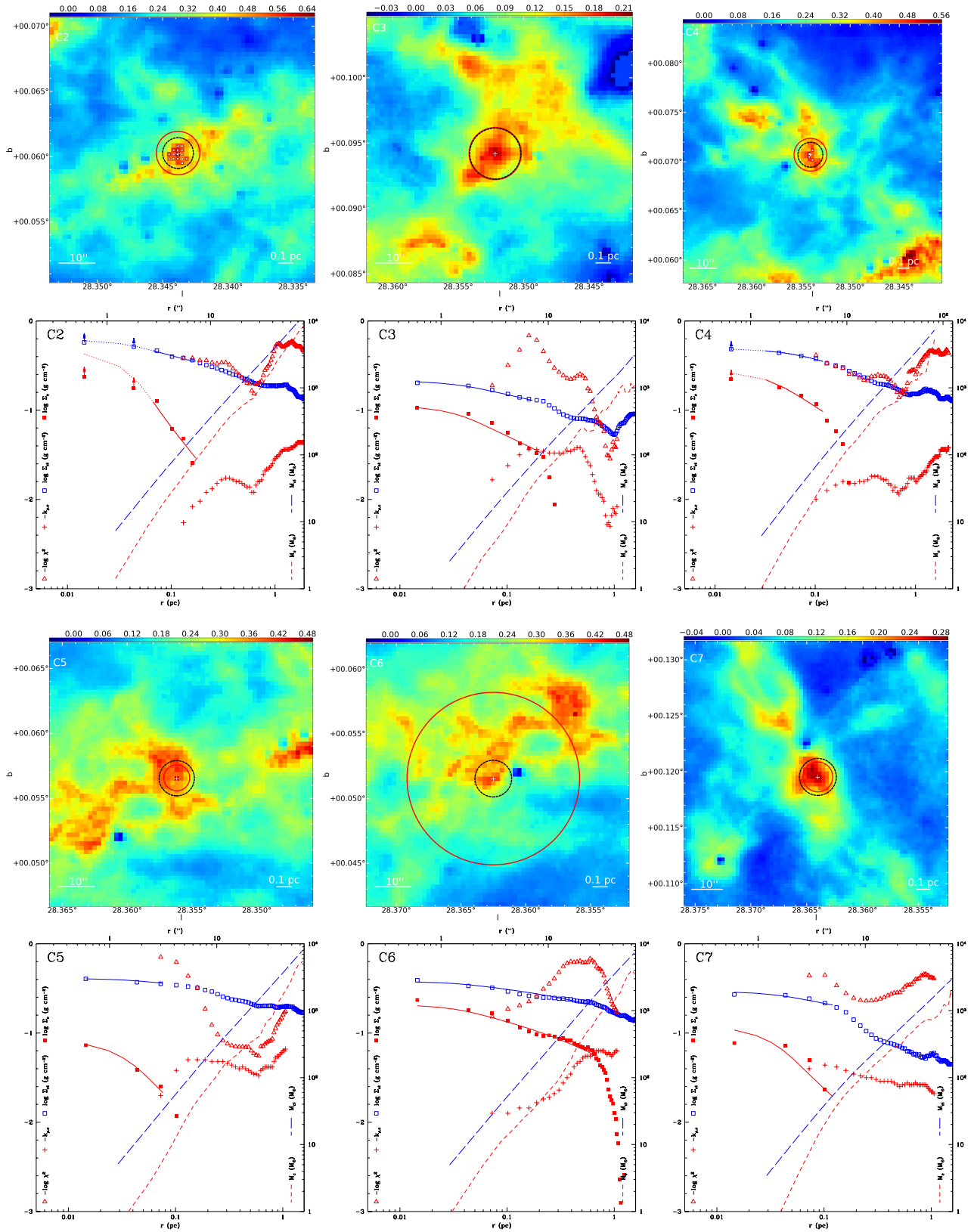


FIG. 7.— Core C2, C3, C4, C5, C6, C7 Σ maps (notation as Fig. 5a) and azimuthally averaged radial profile figures (notation as Fig. 5b).

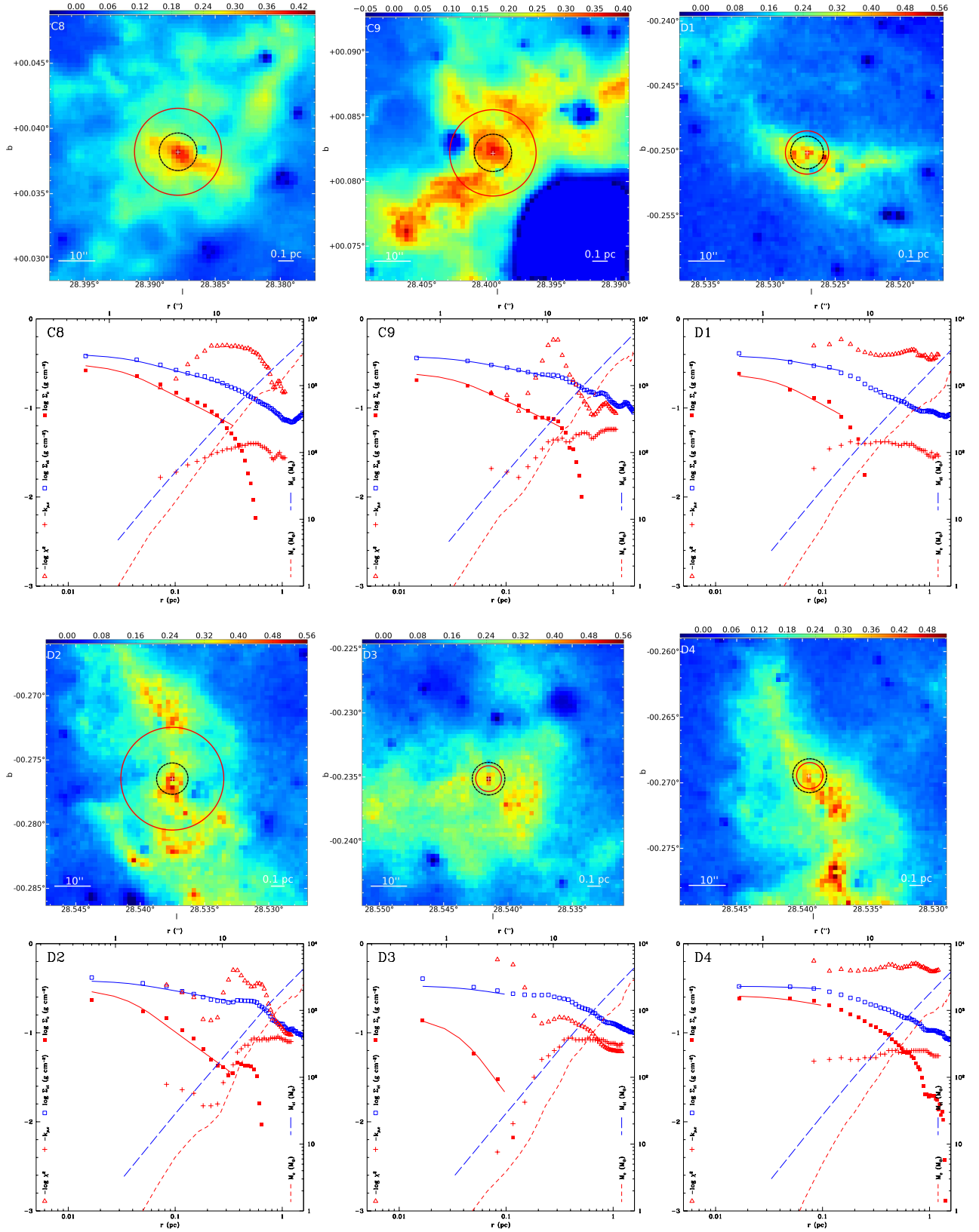


FIG. 8.— Core C8, C9, D1, D2, D3, D4 Σ maps (notation as Fig. 5a) and azimuthally averaged radial profile figures (notation as Fig. 5b).

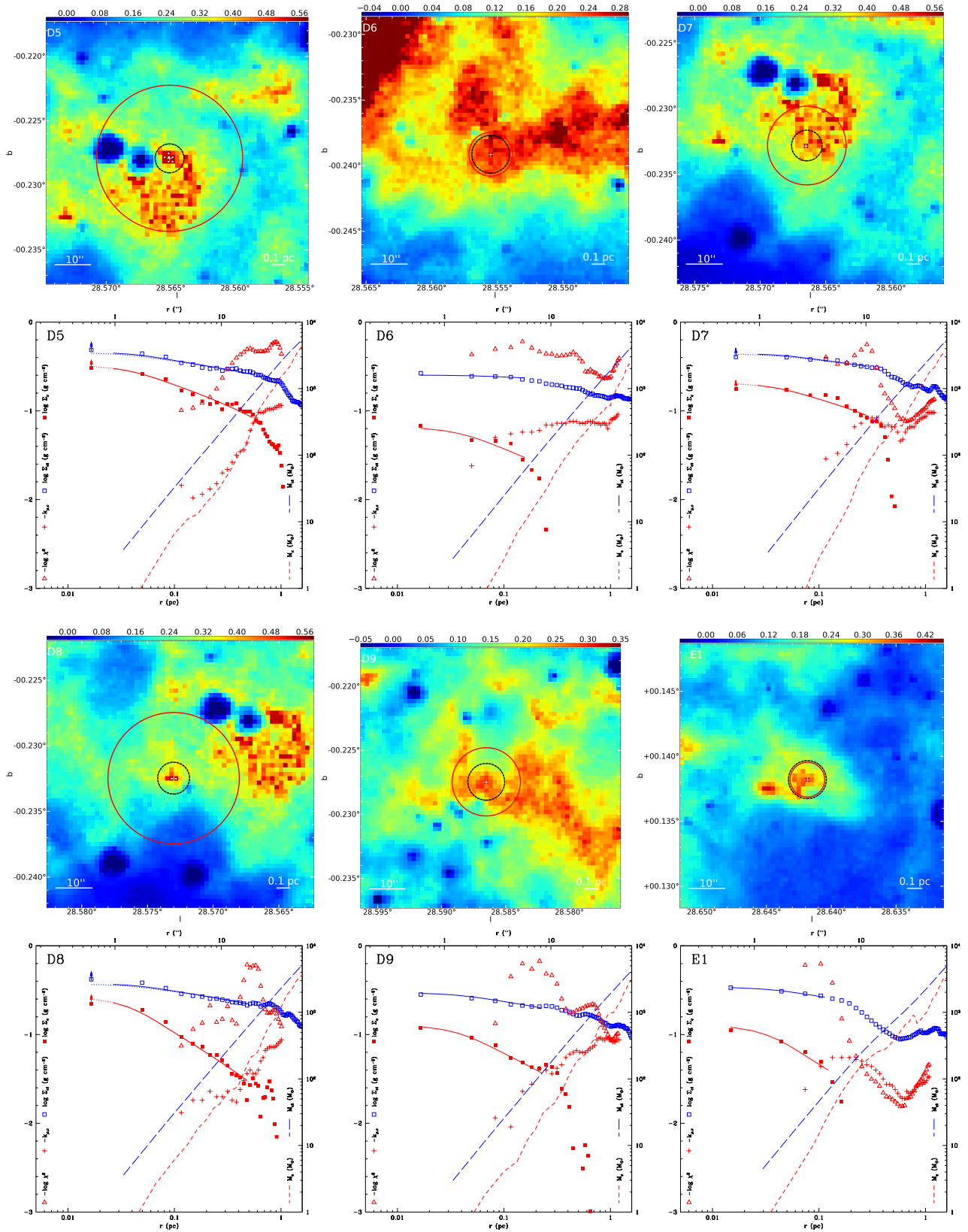


FIG. 9.— Core D5, D6, D7, D8, D9, E1 Σ maps (notation as Fig. 5a) and azimuthally averaged radial profile figures (notation as Fig. 5b).

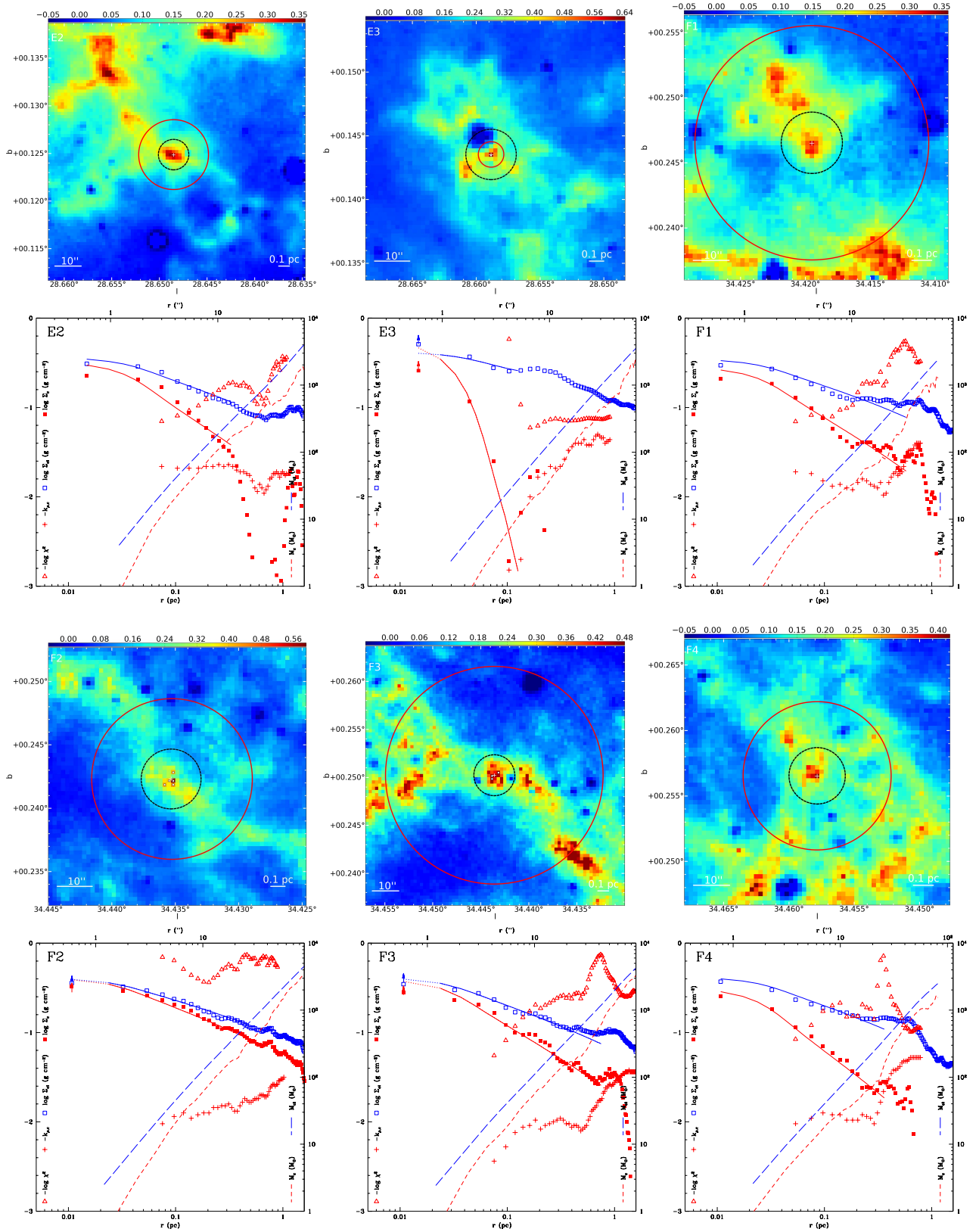


FIG. 10.— Core E2, E3, F1, F2, F3, F4 Σ maps (notation as Fig. 5a) and azimuthally averaged radial profile figures (notation as Fig. 5b).

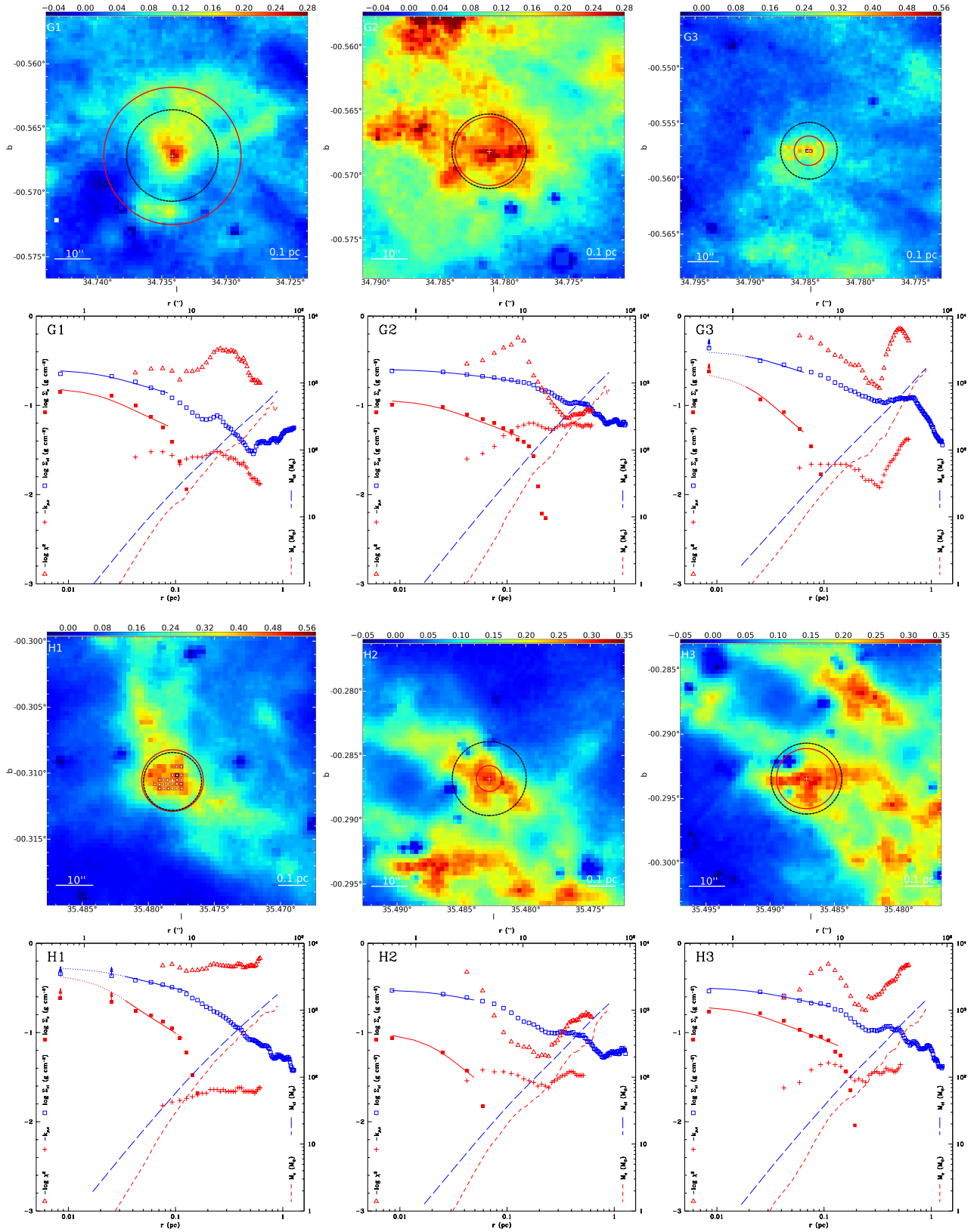


FIG. 11.— Core G1, G2, G3, H1, H2, H3 Σ maps (notation as Fig. 5a) and azimuthally averaged radial profile figures (notation as Fig. 5b).

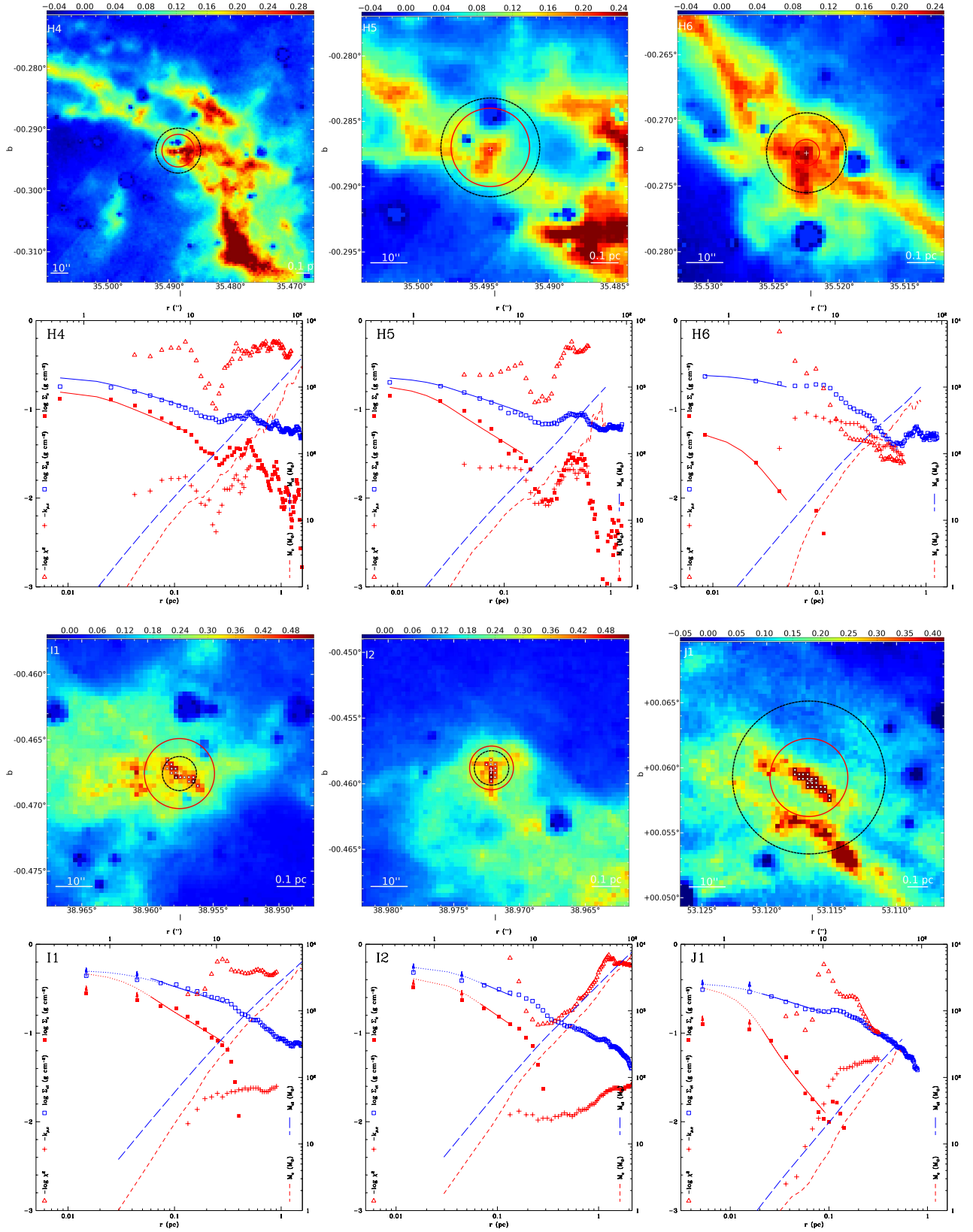


FIG. 12.— Core H4, H5, H6, I1, I2, J1 Σ maps (notation as Fig. 5a) and azimuthally averaged radial profile figures (notation as Fig. 5b).

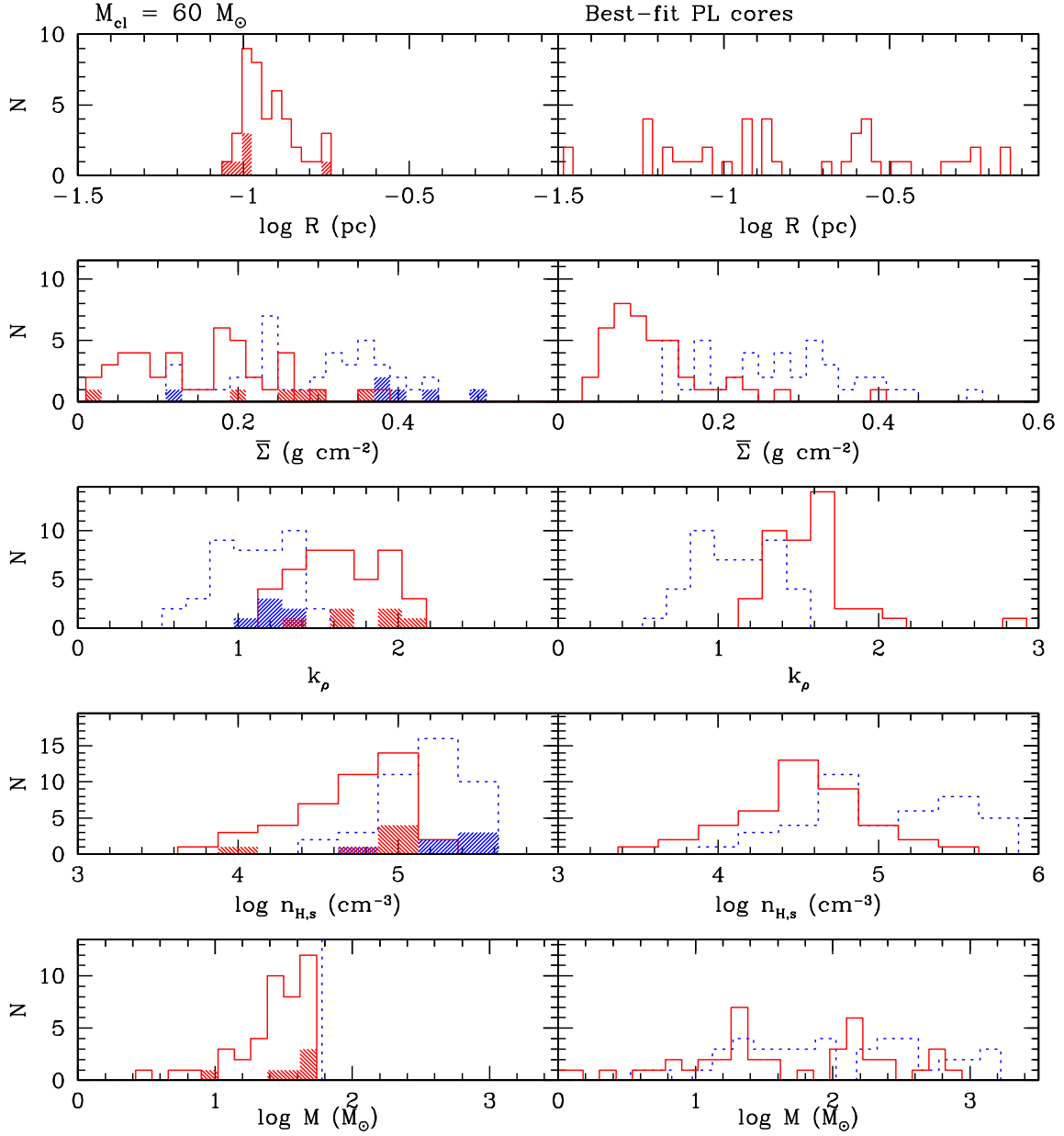


FIG. 13.— (a) *Left column*: Distributions of properties of clumps and cores at the scale where the observed total enclosed mass $M_{\text{cl}} = 60 M_{\odot}$, which defines $R_{\text{cl}} = R_c$. The first graph shows the distribution of R_{cl} (red solid line) of the 42 cores enclosing this mass. The shaded subset shows the 5 cores (A1, C2, H1, I1, I2) that have extended saturation in their centers on this scale. The second panel down shows the mean mass surface density of the clumps, $\bar{\Sigma}_{\text{cl}}$ (blue dotted line; shaded subset as before), and cores after clump envelope subtraction, $\bar{\Sigma}_{\text{c,PL}}$ (red solid line), based on the power law fit. The third panel down shows the distributions of $k_{\rho,\text{cl}}$ (blue dotted line) and $k_{\rho,c}$ (red solid line). The fourth panel shows the distributions of $n_{\text{H},s,\text{cl}}$ (blue dotted line) and $n_{\text{H},s,c}$ (red solid line). The bottom panel shows the distribution of $M_{\text{c,PL}}$ (red solid line). The vertical blue dotted line shows the $60 M_{\odot}$ scale of the clump. (b) *Right column*: As for (a) but now for the best-fit power law plus clump envelope models. The only difference is that in the bottom panel, the clump mass, M_{cl} , is now shown (blue dotted line).

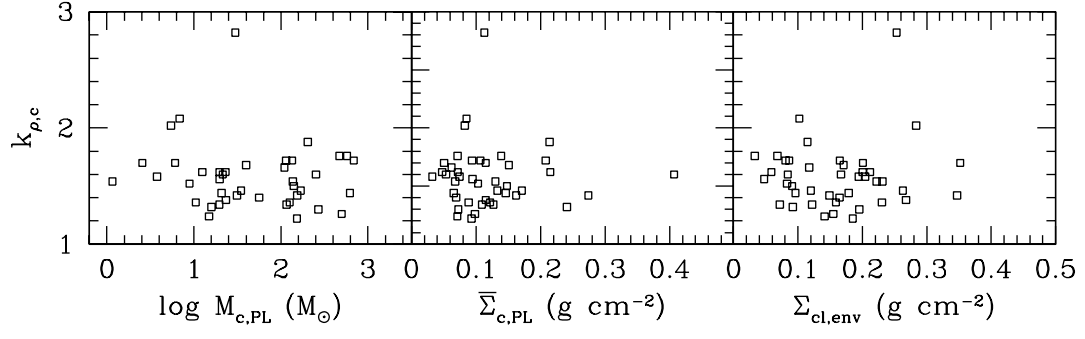


FIG. 14.— $k_{\rho,c}$ versus $M_{c,PL}$, $\bar{\Sigma}_{c,PL}$ and $\Sigma_{cl,env}$ for the best-fit cores.

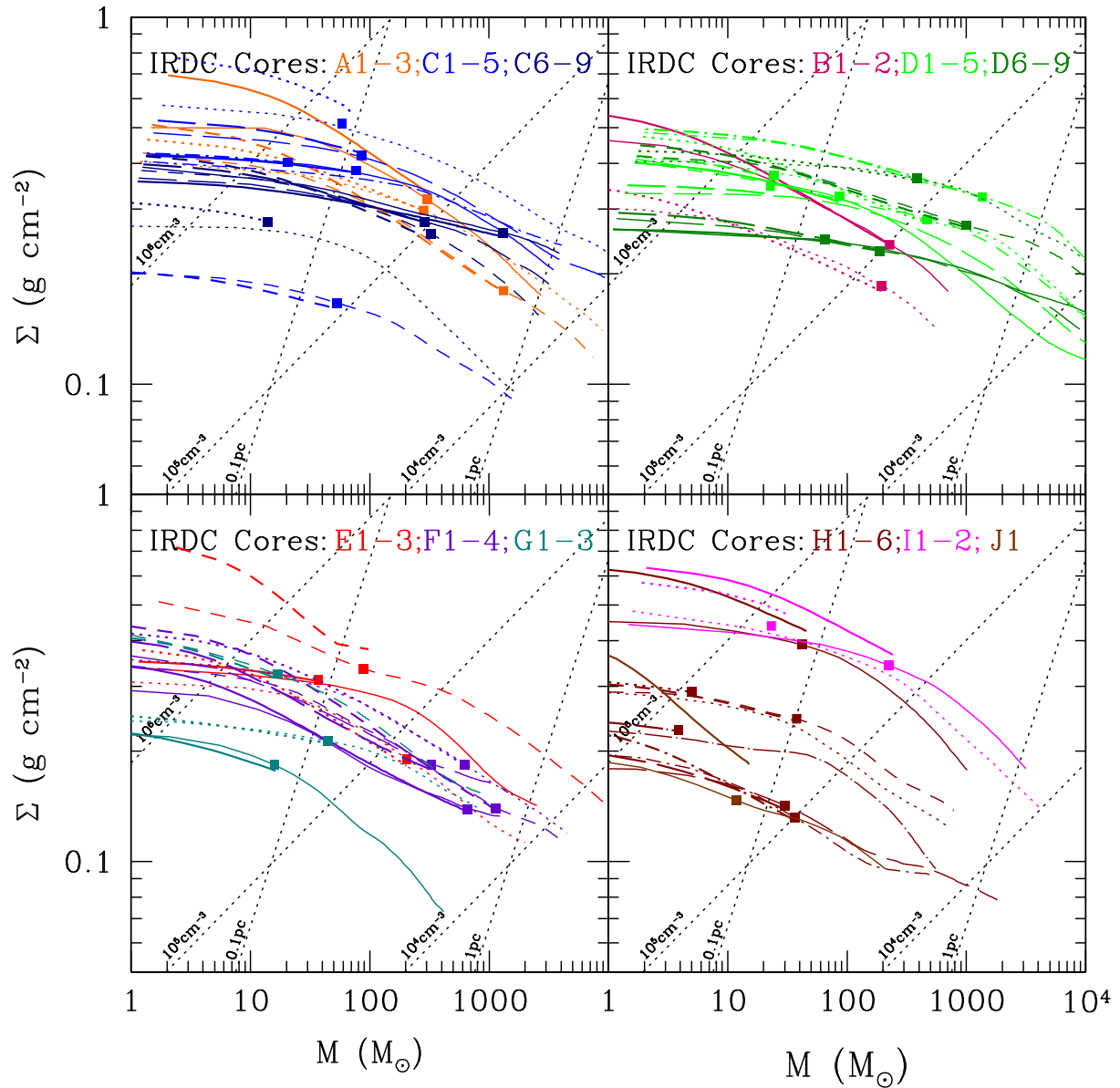


FIG. 15.— Mass surface density versus mass ($\Sigma - M$) diagram (including lines of constant radial size and density $[n_{\text{H}}]$ for spherical clouds) for the 42 IRDC core/clumps. For each range of core numbers, the total mass surface density, Σ_{cl} , of the cores are indicated by color-coded thin solid, dotted, dashed, long-dashed, dot-dashed, dot-long-dashed lines in order of increasing number (e.g. C1 (solid) to C5 (dot-dashed); C6 (solid) to C9 (long-dashed)). Squares mark the location of the best-fit cores. Heavier lines extend inward from near the squares show $\Sigma_{\text{c,PL}} + \Sigma_{\text{cl,env}}$, i.e. based on the fitted power law density profile.

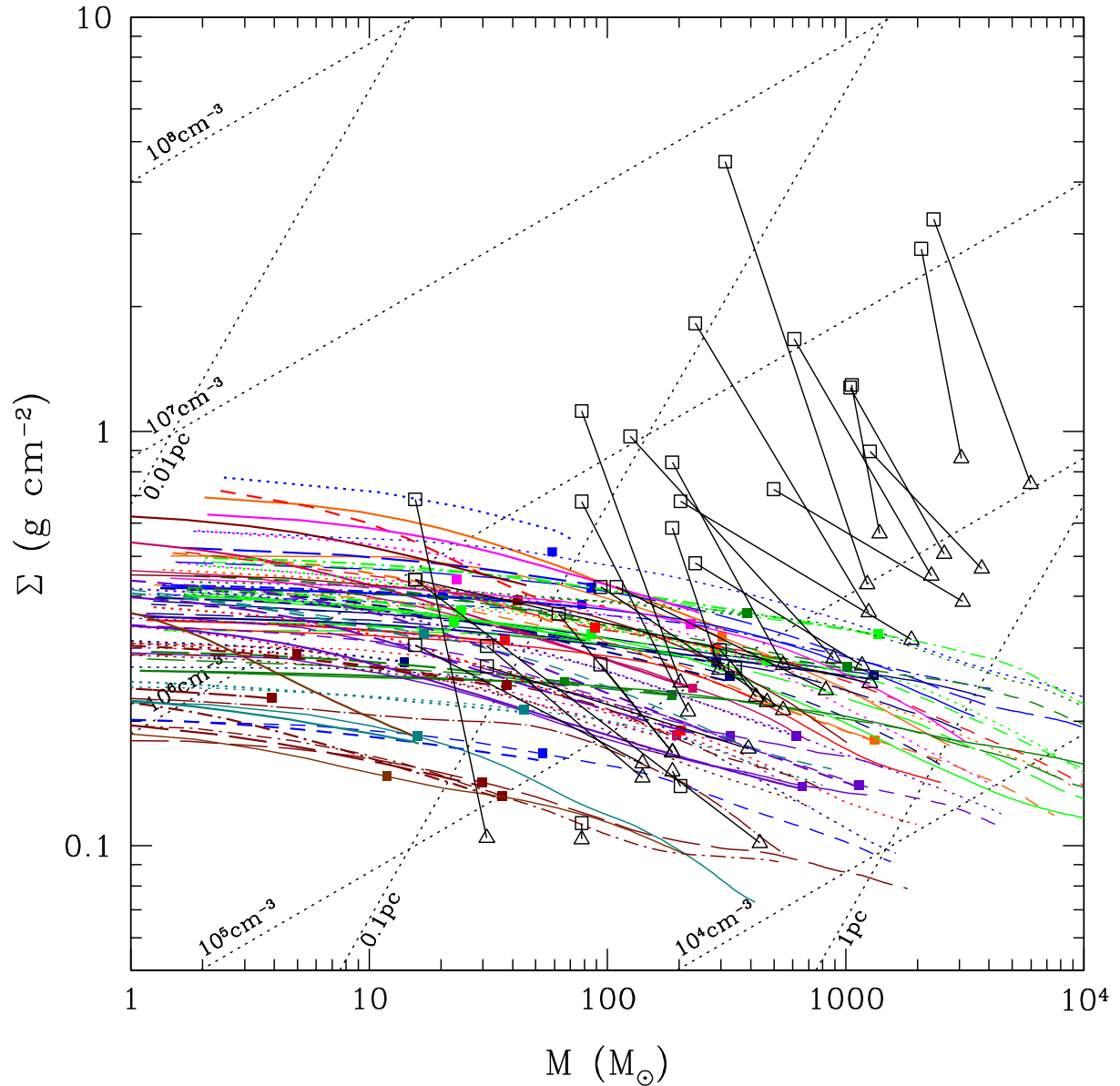


FIG. 16.— Same as Fig. 15, now combining all 42 cores together (colored lines). The black symbols and lines show the masses of 31 actively star-forming core/clumps from Mueller et al. (2002), with triangles indicating the masses above a density threshold of $n_{\text{H}} \sim 3 \times 10^4 \text{cm}^{-3}$ (we have scaled the masses by a factor 1.56 to be consistent with our adopted gas-to-dust mass ratio) and the squares indicating the masses inside the deconvolved source size. Note, the properties of the clouds on this inner scale are not directly resolved, but are inferred based on simple 1D radiative transfer modeling. The IRDC cores/clumps overlap only with the lower- Σ range of the star-forming core/clump sample, perhaps indicating there is an evolutionary growth in core/clump density as star formation proceeds.

TABLE 1
INFRARED DARK CLOUD SAMPLE^a

Cloud Name	l °	b °	d kpc	R_{eff} pc	e	P.A. °	$\bar{I}_{\nu,0,\text{obs}}$ ^b MJy/sr	$f_{\nu,\text{fore}}$	$f_{\nu,\text{fore}}^{\text{BT09}}$	$\Sigma(\text{sat})$ g/cm ²	$\bar{\Sigma}_{\text{SMF}}^c$ g/cm ²	$\bar{\Sigma}_{\text{SMF}}^{\text{BT09}}$ g/cm ²	M_{SMF} M_{\odot}	$M_{\text{SMF}}^{\text{BT09}}$ M_{\odot}
A (G018.82−00.28)	18.822	−0.285	4.8	10.4	0.961	74	93.8	0.472	0.209	0.496	0.0489	0.0355	17,700	7,600
B (G019.27+00.07)	19.271	0.074	2.4	2.71	0.977	88	85.1	0.452	0.075	0.488	0.0814	0.0387	2,200	830
C (G028.37+00.07)	28.373	0.076	5.0	15.4	0.632	78	89.9	0.339	0.266	0.520	0.0610	0.0527	45,000	42,000
D (G028.53−00.25)	28.531	−0.251	5.7	16.9	0.968	60	71.5	0.559	0.327	0.436	0.0525	0.0418	53,400	27,000
E (G028.67+00.13)	28.677	0.132	5.1	11.5	0.960	103	96.7	0.455	0.276	0.504	0.0593	0.0543	25,200	19,400
F (G034.43+00.24)	34.437	0.245	3.7 ^d	3.50	0.926	79	48.4	0.601	0.193	0.370	0.0994	0.0371	4,460	1,670
G (G034.77−00.55)	34.771	−0.557	2.9	3.06	0.953	95	43.2	0.624	0.140	0.347	0.0648	0.0420	2,010	1,140
H (G035.39−00.33)	35.395	−0.336	2.9	9.69	0.951	59	45.6	0.405	0.142	0.416	0.0479	0.0262	13,340	6,800
I (G038.95−00.47)	38.952	−0.475	2.7	3.73	0.917	64	42.1	0.418	0.141	0.402	0.0707	0.0616	2050	1,490
J (G053.11+00.05)	53.116	0.054	1.8	0.755	0.583	50	28.6	0.509	0.121	0.328	0.125	0.0699	259	80

^a Coordinate Names, Galactic coordinates, kinematic distances, effective radii (of equal area circles), eccentricities and position angles of fitted ellipses are from Simon et al. (2006). We then compare quantities derived in this paper with those from BT09.

^b Mean intensity of the SMF background model (BT09) inside the Simon et al. (2006) ellipse.

^c Areal average of those pixels for which values of $\Sigma_{\text{SMF}} > 0$ are derived. Estimates of a mean mass surface density based on M_{SMF} and R_{eff} are typically much smaller because of the regions inside the clouds ellipse with derived $\Sigma_{\text{SMF}} \leq 0$ (see BT09).

^d The distance to IRDC F has recently been estimated from parallax of radio sources to be 1.56 ± 0.12 kpc (Kurayama et al. 2011), a factor of 0.42 smaller than the kinematic distance of Simon et al. (2006). For consistency with BT09, we retain the kinematic distance, but the mass of this cloud and its cores are likely to need to be reduced by a factor of 0.178.

TABLE 2
CORE PROPERTIES

Core ^a	l	b	$R_{cl} = R_c$ pc	Σ_{cl} g/cm ²	Σ_c g/cm ²	$k_{\rho,cl}$	$k_{\rho,c}$	$M_{cl} = 60M_{\odot}$ 10^3 cm^{-3}	$n_{H,s,cl}$ 10^5 cm^{-3}	M_c M_{\odot}	$M_{c,PL}$ M_{\odot}	$\Sigma_{c,PL}$ g/cm ²	R_c pc	$\Sigma_{cl,2}$ g/cm ²	Σ_c g/cm ²	Best-fit		Power Law		$n_{H,s,cl}$ 10^5 cm^{-3}	$n_{H,s,c}$ 10^5 cm^{-3}	M_{cl} M_{\odot}	M_c M_{\odot}	$M_{c,PL}$ M_{\odot}	$\Sigma_{c,PL}$ g/cm ²
																$k_{\rho,cl}$	$k_{\rho,c}$	$k_{\rho,cl}$	$k_{\rho,c}$						
A1 ^m	18.78675	-0.28592	0.0962	0.431	0.316	1.40	2.04	2.47	1.21	37.9	49.2	0.353	0.251	0.319	0.204	1.38	1.88	0.713	0.332	303	194	204	0.214		
A2 ^s	18.80117	-0.29625	0.106	0.356	0.205	1.30	1.79	1.96	0.838	34.6	35.9	0.214	0.251	0.298	0.149	1.34	1.42	0.682	0.353	283	141	154	0.162		
A3 ^s	18.80750	-0.30550	0.109	0.336	0.249	1.46	2.06	1.64	0.767	44.3	46.0	0.0936	0.698	0.180	0.0936	1.48	1.72	0.135	0.0594	1320	686	687	0.0937		
B1 ^m	19.28758	0.08083	0.114	0.307	0.216	1.26	1.68	1.61	0.872	42.1	42.6	0.218	0.251	0.240	0.149	1.28	1.50	0.570	0.307	228	142	141	0.148		
B2	19.30758	0.06625	0.134	0.222	0.151	1.10	1.43	1.08	0.579	40.7	38.6	0.144	0.265	0.185	0.113	1.12	1.34	0.452	0.237	195	120	116	0.109		
C1	28.32450	0.06655	0.102	0.383	0.119	0.900	1.31	2.72	0.677	18.6	18.5	0.118	0.116	0.382	0.114	0.900	1.38	2.40	0.558	77.8	23.3	23.4	0.115		
C2 ^m	28.34383	0.06017	0.0884	0.510	0.164	1.20	1.96	3.59	0.453	19.2	13.1	0.111	0.0872	0.512	0.165	1.26	1.42	3.53	1.71	58.6	18.9	31.3	0.274		
C3	28.35217	0.09450	0.155	0.165	0.0686	1.08	1.45	0.711	0.228	24.9	23.9	0.0659	0.145	0.167	0.0707	1.08	1.44	0.773	0.244	53.4	22.5	20.8	0.0654		
C4 ^s	28.35417	0.07067	0.0958	0.434	0.171	1.09	1.80	2.99	1.67	49.5	53.3	0.386	0.116	0.421	0.158	1.22	1.46	2.24	0.789	85.8	32.2	34.8	0.171		
C5	28.35617	0.05650	0.104	0.369	0.0372	0.781	1.30	2.72	0.188	6.04	5.43	0.0335	0.0581	0.403	0.0512	0.800	1.70	5.28	0.390	20.5	2.60	2.56	0.0504		
C6	28.36267	0.05150	0.109	0.334	0.177	0.904	1.82	2.13	0.718	31.7	34.3	0.192	0.581	0.258	0.103	0.860	1.26	0.330	0.102	1317	524	501	0.0985		
C7	28.36433	0.11950	0.129	0.238	0.0556	1.15	1.45	1.18	0.718	49.2	43.3	0.172	0.0581	0.277	0.0727	1.04	1.58	3.23	0.629	14.1	3.70	3.78	0.0744		
C8	28.38783	0.03817	0.111	0.322	0.202	1.16	1.58	1.85	0.895	37.5	37.5	0.202	0.290	0.257	0.137	1.16	1.46	0.567	0.245	327	175	169	0.133		
C9	28.39950	0.08217	0.111	0.321	0.160	1.02	1.62	1.99	0.705	29.8	30.4	0.163	0.261	0.277	0.118	1.02	1.36	0.732	0.267	286	121	126	0.122		
D1	28.52717	-0.25033	0.109	0.337	0.167	0.956	1.39	2.17	0.885	29.7	31.0	0.178	0.133	0.325	0.154	0.960	1.68	1.71	0.514	86.0	40.9	39.9	0.151		
D2	28.53750	-0.27650	0.105	0.361	0.172	0.873	1.77	2.53	0.720	28.6	29.5	0.0622	0.332	0.280	0.0949	0.860	1.22	0.623	0.171	464	156	153	0.0930		
D3	28.54150	-0.23517	0.110	0.331	0.0608	0.788	1.55	2.29	0.280	11.0	11.2	0.243	0.0663	0.370	0.0863	0.720	2.02	4.38	0.422	24.4	5.71	5.46	0.0825		
D4 ^p	28.53950	-0.26950	0.112	0.318	0.231	0.772	1.29	2.18	1.27	43.5	45.7	0.262	0.0663	0.346	0.254	0.720	1.32	4.10	2.10	22.8	16.8	15.9	0.241		
D5 ^m	28.56533	-0.22783	0.0948	0.443	0.259	0.880	1.92	3.43	1.03	35.1	35.4	0.0461	0.531	0.324	0.145	0.880	1.44	0.445	0.148	1370	614	619	0.146		
D6	28.55550	-0.23917	0.126	0.250	0.0495	0.586	1.24	1.66	0.222	11.9	11.0	0.188	0.133	0.249	0.0486	0.700	1.62	1.48	0.168	66.0	12.8	12.5	0.0475		
D7 ^s	28.56667	-0.23300	0.0993	0.404	0.168	0.559	1.28	3.43	1.12	24.9	27.9	0.171	0.265	0.364	0.133	0.640	1.54	1.12	0.247	385	141	137	0.130		
D8 ^s	28.57283	-0.23267	0.104	0.369	0.169	0.900	1.68	2.57	0.747	27.6	27.7	0.0862	0.497	0.271	0.0756	0.840	1.30	0.408	0.0856	1010	281	269	0.0724		
D9	28.58667	-0.22767	0.126	0.250	0.0832	0.834	1.50	1.49	0.355	19.9	20.6	0.0701	0.232	0.231	0.0664	0.840	1.40	0.743	0.165	187	53.8	56.1	0.0693		
E1	28.64350	0.13817	0.115	0.301	0.0736	0.947	1.26	1.86	0.383	14.6	14.6	0.0735	0.0890	0.313	0.0826	0.940	1.36	2.50	0.561	37.3	9.85	10.5	0.0886		
E2	28.64850	0.12483	0.127	0.246	0.164	1.33	1.66	1.12	0.678	42.2	45.1	0.185	0.267	0.190	0.109	1.38	1.72	0.399	0.177	204	117	115	0.107		
E3 ^m	28.65883	0.14350	0.106	0.352	0.0983	0.980	1.78	2.33	1.35	16.7	29.9	0.176	0.0890	0.335	0.0818	1.48	2.82	4.41	0.175	89.1	21.8	29.9	0.113		
F1	34.41950	0.24583	0.141	0.199	0.114	1.36	1.91	0.806	0.317	34.4	35.5	0.118	0.559	0.139	0.0549	1.34	1.60	0.143	0.0466	658	258	283	0.0537		
F2 ^p	34.43517	0.24217	0.118	0.284	0.251	1.36	1.90	1.37	0.828	53.0	53.8	0.255	0.473	0.184	0.151	1.32	1.76	0.227	0.126	622	512	468	0.139		
F3 ^m	34.44383	0.24967	0.127	0.248	0.178	1.50	2.01	1.01	0.513	43.2	46.2	0.191	0.731	0.140	0.0718	1.46	1.76	0.102	0.0419	1133	578	575	0.0714		
F4	34.45800	0.25650	0.128	0.241	0.122	1.31	1.98	1.11	0.322	30.4	28.8	0.116	0.344	0.184	0.0664	1.36	1.66	0.304	0.0832	329	118	110	0.0620		
G1	34.73417	-0.56683	0.171	0.135	0.0723	1.38	1.54	0.446	0.303	46.3	45.2	0.102	0.0759	0.184	0.101	1.20	1.52	1.50	0.694	15.9	8.72	8.93	0.103		
G2	34.78117	-0.56817	0.138	0.209	0.0674	0.860	1.20	1.12	0.289	19.3	18.4	0.0642	0.118	0.213	0.0717	0.860	1.24	1.34	0.366	44.8	15.0	14.9	0.0710		
G3 ^m	34.78483	-0.55750	0.122	0.270	0.0910	1.25	1.67	1.32	0.756	47.1	44.9	0.203	0.0591	0.324	0.123	1.10	1.70	3.59	0.878	17.0	6.46	6.07	0.115		
H1 ^m	35.47800	-0.31033	0.103	0.377	0.166	1.26	1.68	2.19	0.849	26.4	30.6	0.193	0.0843	0.392	0.180	1.20	1.62	2.90	1.21	42.0	19.3	23.0	0.215		
H2	35.48283	-0.28700	0.137	0.212	0.0496	1.19	1.55	0.970	0.0872	14.0	6.73	0.0238	0.0337	0.290	0.0680	1.02	1.54	5.91	1.01	4.97	1.16	1.16	0.0679		
H3	35.48733	-0.29367	0.131	0.232	0.111	1.08	1.45	1.17	0.437	28.6	27.6	0.107	0.101	0.245	0.123	1.06	1.34	1.63	0.725	37.8	19.0	19.6	0.127		
H4	35.48867	-0.28383	0.177	0.126	0.0785	1.34	2.02	0.412	0.148	37.2	36.6	0.0773	0.118	0.142	0.0943	1.36	1.56	0.686	0.398	29.9	19.7	19.8	0.0945		
H5	35.49450	-0.28733	0.183	0.119	0.0605	1.32	2.04	0.378	0.0986	30.3	27.4	0.0546	0.134	0.132	0.0730	1.30	1.62	0.587	0.258	36.2	20.0	19.6	0.0718		
H6	35.52250	-0.27250	0.145	0.188	0.0166	0.906	1.14	0.947	0.0478	5.28	3.41	0.0107	0.0337	0.228	0.0337	0.900	1.58	4.93	0.471	3.91	0.578	0.553	0.0323		
I1 ^m	38.95783	-0.46783	0.101	0.393	0.227	1.21	1.72	2.39	1.27	34.7	44.6	0.292	0.207	0.343	0.178	1.24	1.72	1.01	0.447	223	116	135	0.208		
I2 ^s	38.97217	-0.45950	0.102	0.384	0.227	1.32	1.92	2.18	0.933	35.4	39.9	0.256	0.0593	0.439	0.272	1.54	1.60	3.73	3.31	23.2	14.4	21.5	0.407		
J1 ^m	53.11683	0.05917	0.179	0.123	0.0282	0.992	1.34	0.482	0.105	13.7	15.9	0.0327	0.0733	0.147	0.0447	1.18	2.08	1.26	0.369	11.9	3.61	6.88	0.0852		

^a Core designation from BT09. ^s indicates core is saturated; ^p indicates core's central position has been moved out of the original core boundary from Rathborne et al. (2006); ^m indicates the intensity minimum within the IRDC boundary occurs in this core.

TABLE 3
PROPERTIES OF IRDC CORE AND CLUMP SAMPLE

Mass Scale	Property	Mean	Median	Dispersion
$M_{\text{cl}}(< r) = 60 M_{\odot}^{\text{a}}$	$R_{\text{cl}} = R_c$ (pc)	0.121	0.114	0.0238
...	Σ_{cl} (g cm^{-2})	0.296	0.318	0.0952
...	$k_{\rho,\text{cl}}$	1.09	1.10	0.236
...	$n_{\text{H},\text{s,cl}}$ (10^5cm^{-3})	1.76	1.85	0.852
...	M_c (M_{\odot})	30.4	30.4	12.7
...	Σ_c (g cm^{-2})	0.139	0.160	0.0738
...	$k_{\rho,c}$	1.64	1.67	0.271
...	$n_{\text{H},\text{s,c}}$ (10^5cm^{-3})	0.639	0.750	0.394
...	$M_{\text{c,PL}}$ (M_{\odot})	31.1	31.0	13.5
...	$\Sigma_{\text{c,PL}}$ (g cm^{-2})	0.154	0.171	0.0899
Best-fit PL+env. ^b	M_{cl} (M_{\odot})	279	86.0	392
...	R_c (pc)	0.222	0.134	0.187
...	Σ_{cl} (g cm^{-2})	0.274	0.277	0.0925
...	$k_{\rho,\text{cl}}$	1.10	1.12	0.246
...	$n_{\text{H},\text{s,cl}}$ (10^5cm^{-3})	1.76	1.12	1.63
...	M_c (M_{\odot})	128	32.2	185
...	Σ_c (g cm^{-2})	0.113	0.103	0.0535
...	$k_{\rho,c}$	1.58	1.56	0.277
...	$n_{\text{H},\text{s,c}}$ (10^5cm^{-3})	0.515	0.354	0.616
...	$M_{\text{c,PL}}$ (M_{\odot})	128	34.8	181
...	$\Sigma_{\text{c,PL}}$ (g cm^{-2})	0.121	0.107	0.0708

^a Mass scale set by the enclosed mass in the Σ map being equal to $60 M_{\odot}$.

^b Mass scale set by the best-fit power law plus clump envelope model.